Article:
Mernild, S.H., Liston, G.E., Hiemstra, C. et al. (2017) The Andes Cordillera. Part IV: spatio-temporal freshwater run-off distribution to adjacent seas (1979-2014). International Journal of Climatology, 37 (7). pp. 3175-3196. ISSN: 0899-8418

https://doi.org/10.1002/joc.4922

The Andes Cordillera. Part IV: Spatiotemporal freshwater runoff distribution to adjacent seas (1979–2014)

SEBASTIAN H. MERNILD

Antarctic and Sub-Antarctic Program, Universidad de Magallanes, Punta Arenas, CHILE, and Faculty of Engineering and Science, Sogn og Fjordane University College, Sogndal, NORWAY

GLEN E. LISTON

Cooperative Institute for Research in the Atmosphere, Colorado State University, Fort Collins, Colorado, USA

CHRISTOPHER HIEMSTRA

U.S. Army Cold Regions Research and Engineering Laboratory, Ft. Wainwright, Alaska, USA

ANDREW P. BECKERMAN

Department of Animal and Plant Sciences, University of Sheffield, UK

JACOB C. YDE

Faculty of Engineering and Science, Sogn og Fjordane University College, Sogndal, NORWAY

JAMES McPHEE

Department of Civil Engineering and Advanced Mining Technology Center, Facultad de Ciencias Fisicas y Matemáticas, Universidad de Chile, CHILE

Accepted International Journal of Climatology, 27 September, 2016

Corresponding author address:

Dr. Sebastian H. Mernild, e-mail: sebastian.mernild@hisf.no

Abstract

The spatiotemporal freshwater river runoff pattern from individual basins, including their runoff magnitude and change (1979/80–2013/14), was simulated for the Andes Cordillera west of the Continental Divide in an effort to understand runoff variations and freshwater fluxes to adjacent fjords, Pacific Ocean, and Drake Passage. The modeling tool SnowModel/HydroFlow was applied to simulate river runoff at 3-hour intervals to resolve the diurnal cycle and at 4-km horizontal grid increments using atmospheric forcing from NASA Modern-Era Retrospective Analysis for Research and Applications (MERRA) datasets. Simulated river runoff hydrographs were verified against independent observed hydrographs. For the domain, 86 % of the simulated runoff originated from rain, 12 % from snow melt, and 2 % from ice melt, where for Chile, the water-source distribution was 69 %, 24 %, and 7 %, respectively. Along the Andes Cordillera the 35-year mean basin-outlet specific runoff (L s^{-1} km^{-2}) showed a characteristic regional hourglass shape pattern with highest runoff in both Colombia and Ecuador and in Patagonia, and lowest runoff in the Atacama Desert area. An Empirical Orthogonal Function analysis identified correlations between the spatiotemporal pattern of runoff and flux to the El Niño Southern Oscillation Index (ENSO) and to the Pacific Decadal Oscillation (PDO).

KEYWORDS: Andes Cordillera; Freshwater runoff; HydroFlow; Modeling; NASA MERRA; river; South America

1. Introduction

River runoff integrates a response of the watershed to precipitation, snow and glacier presence, groundwater flow, and other hydrometeorological processes (e.g., Liston and Mernild 2012; Bliss et al. 2014). Snow, glaciers, and underground reservoirs store and release melt water on a range of time scales that control down-stream river runoff regimes (Jansson et al. 2003; Hock et al. 2005; Bliss et al. 2014). In most cases, the largest meltwater contribution occurs during annual springtime snowmelt. On a longer timescale of years, glaciers represent a longer-term storage influenced by warmer periods when mass-balances are negative, or cooler periods when they are positive. Given shifts in snow and rain contributions (Barnett et al. 2005; Kapnick and Hall, 2012) as well as glacial mass balances (Vaughan et al. 2013), accurate estimates of snow and glacial melt inputs to the hydrological budget are needed.

For South America, modeling tools offer potential to enhance the limited streamflow observational record at high elevation Andean river basins. For 50 river basins in Colombia, Poveda et al. (2001) emphasized that the effects of coarse-scale natural atmospheric variability above the Pacific Ocean – the multivariate El Niño Southern Oscillation (ENSO) (Wolter and Timlin 2011) – are stronger for river runoff than for precipitation, owing to concomitant effects of soil moisture content and evapotranspiration. However, between latitudes 30°S and 35°S, El Niño events have a strong tendency to be positively linked to annual precipitation, and negatively linked during La Niña events (Rutllant and Fuenzalida 1991; Escobar et al. 1995; Montecinos and Aceituno 2002; Garreaud 2009; Wolter and Timlin 2011).

Fleischbein et al. (2006) estimated the water budget for three river basins in Ecuador (4°S) (1998–2002) based on observations and modeled surface flow, and showed that ~40 % of the runoff came from rainfall. Crespo et al. (2011) analyzed the rainfall–runoff relation of 13

intensively monitored micro-basins in the Andes of southern Ecuador (4°S), and showed that the annual amount of runoff was strongly controlled by rainfall. For the tropical area of the Cordillera Blanca in Peru (9°S), glacier retreat and snow and ice meltwater result in complex hydrological interactions, where glacier retreat, according to Baraer et al. (2012), leads to a decrease in dry-season river runoff. Accurate estimates of snow and glacial melt inputs to the hydrological budget enhance our ability to make predictions about future water resources as glaciers retreat (Gordon et al. 2015).

The primary river runoff source in central Chile and central-western Argentina is snow meltwater (Masiokas et al. 2006; Melo et al. 2010). In Chile, the *Dirección General de Aguas* (DGA; http://dgasatel.mop.cl) operates more than 550 individual stream gages (17–54°S), covering the period from the early 1940s to the present. In the early 1940s, approximately 40 individual hydrographic stations were in operation (18–34°S). The purpose of this monitoring network is to quantify water resource availability at economically relevant river reaches, influenced by different climate conditions along the Chilean Andes Cordillera.

Runoff time series analyses identified ongoing changes in watersheds and their suspected correlates. Rubio-Álvarez and McPhee (2010) analyzed spatiotemporal variability in annual and seasonal river-runoff for 44 rivers with unimpeded flow records in southern Chile (34–45°S; 1952–2003). They suggested that decreasing runoff (37.5–40°S) was correlated with decreasing trends in observed precipitation. Cortés et al. (2011) studied several rivers on the western slope of the Andes Cordillera (1961–2006; 30–40°S), and found that hydrological changes are less apparent for rivers located at higher elevations, despite the fact that temperatures have been steadily rising in the region.

In Chile's Norte Chico region (26–32°S), which contains some of the most glacierized basins of the region besides the Maipo and Chchapola/Tinguirrica Basins, glacier volume loss contributed 5–10 % of the runoff at 3,000 m above sea level (a.s.l.) (Favier et al. 2009). Direct glacier runoff measurements were conducted at the snouts of four glaciers, showing that the mean annual glacier contribution to river runoff ranged between 4–23 % – values which are greater than the glacierized fraction of the basins (Gascoin et al. 2011). In addition, observations of glacier river runoff have been conducted in the Olivares Basin (33°S; 2014–2016) to understand the ratio between snow-derived runoff and basin outlet river runoff (Mernild et al. 2016b).

Despite these regional studies, substantial information about the quantitative spatiotemporal hydrological conditions, including river runoff, of the numerous basins along the Andes Cordillera remains a largely unaddressed gap in our understanding. This is true for the large basins and abundant smaller basins that comprise the Cordillera. These conditions include basin outlet river runoff magnitudes, trends, and ratios between runoff and rain-derived runoff, snow-derived runoff, and ice-derived runoff. Additional coarse-scale – cross country border – analyses can provide much needed insights into the availability of regional water resources, the terrestrial runoff impact on fjord and ocean density, stratification, and coastal circulations, and the subsequent impacts on sea-level rise and other aspects of Earth's climate system. Today, all these issues are poorly known along the Andes Cordillera and our understanding is limited. There is an urgent need for hydrological model simulations to understand the link between a changing climate and the associated changes in terrestrial freshwater runoff and oceanographic conditions along the Andes Cordillera.

120 In this study, SnowModel/HydroFlow (Liston and Mernild 2012; Mernild and Liston
121 2012) were used to simulate hydrological conditions along the Andes Cordillera. These
122 simulations include freshwater river runoff magnitudes and trends, runoff routing, the
123 spatiotemporal distribution of basin outlet river runoff to surrounding fjords and seas, and the
124 ratios between rain-derived runoff, snow-derived runoff, and ice-derived runoff. Down-scaled
125 atmospheric reanalysis data from NASA MERRA was applied using the meteorological
126 algorithms and sub-models implemented within MicroMet (Liston and Elder 2006a) with a 3-
127 hour temporal resolution to simulate river runoff hydrographs and spatiotemporal river basin
128 variability. Direct independent observed river runoff time series for the period 1979–2014 – for
129 specific basins – were used to verify the HydroFlow simulated river hydrograph performance.
130 We simulated, mapped, and analyzed, to our knowledge for the first time, the freshwater
131 runoff representations for glacier, and snow-free and snow-covered land from 1979 through 2014
132 for the entire Andes Cordillera west of the continental divide (Figure 1). This Part IV paper
133 focuses on: 1) linkages among runoff production from land-based liquid precipitation (rain) and
134 snowmelt (Part I and II, Mernild et al. 2016a, 2016b) and ice-melt processes (Part III, Mernild et
135 al. 2016c), and the associated spatiotemporal routing of freshwater river fluxes along the Andes
136 Cordillera to surrounding fjords, the Pacific Ocean and the Drake Passage; 2) latitudinal and
137 seasonal variabilities in river runoff along the Andes Cordillera; and 3) runoff variabilities in
138 relation to large-scale atmospheric circulation patterns. At coarsest scales, the spatiotemporal
139 quantities of freshwater runoff and routing are associated with climactic variability ranging from
140 Patagonian sub-polar latitudes (from Tierra del Fuego) to the cold and high mountain Tropical
141 Andes climate. At finer scales, runoff is driven by heterogeneity in the snow- and ice-covered
142 and snow- and ice-free landscapes. To enhance our overview of runoff patterns and sources, we

applied Empirical Orthogonal Function (EOF) analysis (e.g., Preisendorfer 1998; Sparnocchia et al. 2003; Mernild et al. 2015) to evaluate river runoff variations; estimate contributions of rain-, snow-, and ice-based runoff; and assess correlations between ENSO (Wolter and Timlin 2011) and the Pacific Decadal Oscillation (PDO) (Zhang et al. 1997). These atmospheric circulation indices are good measures of atmospheric flow and moisture transport variability in the South Pacific (e.g., Carrasco et al. 2005; Garreaud 2009; McClung 2013; López-Moreno et al. 2014), and are important variables for terrestrial hydrosphere and cryosphere conditions (e.g., Sagredo and Lowell 2012; Saltzmann et al. 2013; Veettil et al. 2014).

2. Model description, setup, and verification

2.a SnowModel and HydroFlow

In this research, SnowModel (Liston and Elder 2006b) was used to characterize meteorological, snow, and glacier mass-balance processes and conditions (Parts I–III; Mernild et al. 2016a, 2016b, 2016c) and the submodel HydroFlow was applied to describe freshwater river runoff and routing processes. SnowModel is a spatially-distributed meteorological, energy balance, snow, ice evolution, and freshwater runoff routing modeling system incorporating six submodels. Here, five out of the six submodels are used (the data assimilation submodel, *DataAssim*, is not used): *MicroMet* is a quasi-physically based high-resolution meteorological distribution model (Liston and Elder 2006a), *Enbal* is an energy surface exchange and melt model (Liston 1995; Liston et al. 1999), *SnowTran-3D* is a snow surface redistribution by wind model (Liston and Sturm 1998, 2002; Liston et al. 2007), *SnowPack-ML* is a multilayer snowpack model (Liston and Mernild 2012), and *HydroFlow* is a gridded linear-reservoir runoff routing model (Liston and Mernild 2012; Mernild and Liston 2012). In this system, runoff

166 originates from rain, snowmelt that flows from the bottom of the simulated snowpack; and/or ice
167 melt from the bare glacier surface into the supraglacial, englacial, subglacial, and subsequent the
168 proglacial drainage system. When surface melting is simulated by SnowModel, meltwater is
169 assumed to flow instantaneously when the surface is defined as glacier ice. When snow cover is
170 present, the SnowPack-ML runoff routines take both internal retention and refreezing into
171 account when snow melts at the snowpack surface and subsequent melt water penetrates through
172 the snowpack. Such internal snowpack routines have an effect on the runoff lag time, and how
173 long it takes for the freshwater to reach the seas. By not including these internal snowpack
174 routines in SnowPack-ML it would lead to faster outflow of runoff, including an earlier initial
175 seasonal runoff.

176 In HydroFlow, basins are included within a raster and adjacent cells are linked via a
177 topographically controlled flow network (Liston and Mernild 2012). Each grid cell acts as a
178 linear reservoir that transfers water from itself and all upslope cells to the downslope cells within
179 individual drainage basins, and eventually to surrounding fjords and seas. HydroFlow assumes
180 that in each grid cell there are two flow transfer responses: slow and fast (Liston and Mernild
181 2012). Each of these transfer functions is associated with different time scales and represents the
182 wide range of physical processes determining horizontal moisture transport through and across
183 the domain. The slow time scale accounts for the time it takes runoff at each individual grid cell,
184 usually produced from rain and/or snowmelt, to transport within the snow matrices (in the case
185 of glaciers) and soil (for the case of snow-covered and snow-free land) to the routing network.
186 Hereafter, the moisture is transported through a HydroFlow-generated routing network (the
187 subscripts N, NE, E, SE, S, SW, W, and NW indicate the compass direction of the adjacent
188 connecting grid box) where the fast time scale generally represents some kind of channel flow,

189 such as that represented by supraglacial, englacial, or subglacial flow (in the case of glaciers) and
190 river and stream channels (in the case of snow-covered and snow-free land). For each of the two
191 flow responses, the residence-time, or flow velocity, was estimated based on field tracer
192 experiments (Mernild 2006; Mernild et al. 2006; Mernild et al. unpublished data) and the surface
193 slope (Liston and Mernild 2012).
194
195 *2.b Meteorological forcing, model configuration, and simulation domain*
196 The freshwater river runoff routing and the spatiotemporal runoff hydrograph distribution
197 were simulated for the 35-year period from 1 April 1979 through 31 March 2014. The
198 simulations were forced by NASA MERRA data provided on a 2/3° longitude by 1/2° latitude
199 grid at an hourly time step (Bosilovich 2008; Bosilovich et al. 2008, 2011; Cullather and
200 Bosilovich 2011; Rienecker et al. 2011; Robertson et al. 2011). The NASA MERRA data set was
201 aggregated to 3-hour values to resolve the diurnal cycle while improving the computational
202 efficiency (see Mernild et al. (2014; 2016a, Part I) for further information regarding NASA
203 MERRA forcing).
204 The forcing dataset (NASA MERRA) strongly influences SnowModel's simulated values
205 and biases (Liston and Hiemstra 2011). The reanalysis datasets possess uncertainties associated
206 with assimilated observational datasets, temporal data discontinuities, and model physics (e.g.,
207 Bosilovich et al. 2008, 2011; Liston and Hiemstra 2011). As a consequence, simulated
208 meteorological, snow, ice mass-balance, and river runoff characteristics and trends were dictated
209 by the forcings and may be susceptible to biases associated with changes in data streams and
210 observational inputs (for further information see Liston and Hiemstra 2011). Substantial effort
211 has been dedicated to producing and evaluating reanalyzes, and limiting their biases, with

212 precipitation being a key variable of interest (see Bosilovich et al. 2008, 2011; Cullather and
213 Bosilovich 2011). The relatively small number of data streams and observational inputs present
214 during the early part of the simulations does not necessarily imply degradation in simulated
215 meteorological fields. In the analysis that follows, we therefore assume these data increases do
216 not significantly influence the general trends we produce and describe herein.
217 The NASA MERRA forcings were downscaled in MicroMet to create distributed
218 atmospheric fields, where the spatial interpolations were performed using the Barnes objective
219 analysis scheme, and the interpolated fields were adjusted using known temperature–elevation,
220 wind–topography, humidity–cloudiness, and radiation–cloud–topography relationships (Liston
221 and Elder 2006a). Topography data for SnowModel were obtained from the United States
222 Geological Survey's 7.5 arc-second Global Multi-resolution Terrain Elevation Data 2010
223 (GMTED2010; Danielson and Gesch 2011), and rescaled to a 4-km horizontal grid increment.
224 The land cover distribution file was a hybrid dataset created from a 2009 300-m Global Land
225 Cover (GlobCover 2.3, http://ionia1.esrin.esa.int/) for non-glacier areas and from the Randolph
226 Glacier Inventory v. 4.0 for glaciers (Pfeffer et al. 2014). Regarding changes in glacier area,
227 hypsometry, and thinning, SnowModel neglects these influences throughout the simulation
228 period. Instead, SnowModel uses a constant glacier area and elevation defined from datasets
229 produced during the 2000s and 2010, respectively (Mernild et al. 2016c). The use of these
230 constant conditions may result in errors in the simulated surface mass-balances (SMB) budget
231 and runoff, particularly at the beginning of the simulation period. Also, it may neglect a decrease
232 in dry-season river runoff as observed in Cordillera Blanca in Peru (9°S) (Baraer et al. 2012)
233 since glacier area retreat is not accounted for throughout the simulation period.

234 HydroFlow divided the domain into individual drainage basins (Figure 1b), each with its
235 own streamflow network that drains runoff to downslope areas and into the adjacent fjords and
236 seas. For the domain west of the continental divide, HydroFlow generated 4,224 individual
237 basins all draining into fjords connected to The Pacific Ocean or The Drake Passage, or directly
238 into the Pacific Ocean or The Drake Passage (Figure 1a). The individual HydroFlow estimated
239 basins varied in size from 32 to 62,864 km^2 (located near Concepción, Chile; 37ºS), with a mean
240 and median basin size of 294 km^2 and 48 km^2, respectively, where 83 % of the drainage basins
241 cover equal to or less than 100 km^2. These many relatively small basins (<100 km^2) cover 14 %
242 of the total drainage area, where about two-thirds of these basins are located south of the city
243 Puerto Montt (41ºS), Chile.

244

245 *2.c SnowModel and HydroFlow verification*

246 This paper is the fourth in a series of papers about SnowModel MERRA simulations for
247 the Andes Cordillera on climate, snow, glacier mass-balance, and hydrological conditions,
248 including river runoff routing. The simulations presented were verified against independent
249 observational datasets. In Part I (Mernild et al. 2016a), SnowModel-simulated maximum annual
250 snow cover extent, snow depths, and snow density were evaluated against a suite of remote
251 sensing and field observations. The MODIS/Terra Snow Cover Daily L3 Global 500-m grid
252 (MOD10A1) product (Hall et al. 1995, 2006; Hall and Riggs 2007) was used from 2000/01
253 through 2013/14 for validation of maximum annual simulated snow cover extent for a rectangle
254 between 31.5–40.0°S and 69.2–72.3°W, indicating acceptable results (for detailed information
255 about the quantitative model skill metrics, see Mernild et al. 2016a). Additionally, more than
256 three thousand individual observed snow depths and snow densities measured between 30–37°S

for the central Chilean Andes Cordillera (Ayala et al. 2014; Cornwell et al. 2016) were used. These observations cover the period 2010 through 2014 and were recalculated into mean 4-km grid increments identical to the grids used in SnowModel and used for verification of SnowModel grid simulated snow depths and snow densities. Acceptable verification was determined according to the deviation between simulated and observed mean grid snow depth values.

In Part II, for a specific drainage basin – the Olivares Basin (33°S; 548 km^2) – simulated snow cover extent for specific dates, snow line (the snow line is a net product of seasonal accumulation and ablation processes), snow depletion curves, and freshwater runoff for the period 1979–2014 were verified against independent observations, yielding satisfactory results (for detailed information about the quantitative model skill metrics, see Mernild et al. 2016b).

In Part III, simulated glacier SMB time series (1979–2012) were verified against independent direct observed annual glacier SMB time series from seven glaciers (e.g., WGMS 2013; Mernild et al. 2015), having a total of 72 direct observed annual glacier SMB; the seven glaciers are ≥ 1 km^2, equal to the grid increment size used for the glacier SMB simulations. In addition, these simulations were compared with satellite gravimetry and altimetry-derived SMB (Gardner et al. 2013). For the independent SMB datasets, the verification indicated a good agreement between simulations and independent observations (for detailed information about the quantitative model skill metrics, see Mernild et al. 2016c).

SnowModel simulated river runoff values were verified against coincident independently observed river runoff from DGA hydrographic stations in central Chile (28–39°S) (in this study). DGA observed river runoff time series values spanning ≥ 98 % of the 1979–2014 simulation range were chosen for model verification, resulting in 16 comparison pairs covering the latitudes

25–40ºS (Figure 1c and Table 1). As examples, two hydrographic stations, one located at Rio Aconcagua en Chacabuquito (RAC; 30°S) and another at Rio Cautin en Cajon (RCC; 37°S) are illustrated on Figure 2, together with the HydroFlow topographically-controlled flow network for the basins. Daily simulated and observed runoff from all 16 selected hydrographic stations (Figure 3a) shows on average an r^2-value = 0.51, $p < 0.01$ (where r^2 is the explained variance and p is level of significance) and a r^2-range from 0.31–0.71. It indicates that HydroFlow overall was able to account for 51 % of the variance in river runoff at all of the 16 selected hydrographic stations (Table 1). For example, for the stations RAC and RCC the r^2-values were 0.60 ($p < 0.01$) and 0.69 ($p < 0.01$) (Table 1), respectively. Further, we did a Nash–Sutcliffe coefficient (NSC) test (Nash and Sutcliffe 1970) for the 16 selected hydrographic stations, with a mean NSC value of 0.47 and a range from 0.35–0.64. If the NSC is 1, then the model is a perfect fit to the observations. If NSC is less than 1, decreasing values represent a decline in goodness of fit, where 0 and negative values represent major deviations between the modeled and observed data and the observed mean is a better predictor than the model. In Figures 3b and 3c, the simulated and observed hydrograph time series (based on daily values) are shown for both RAC and RCC, indicating similarity between seasonal (intra-annual) variations in simulated and observed river runoff at the two hydrographic stations RAC and RCC (Figure 3c). Overall, the highlighted runoff verifications provide confidence in the simulated runoff time series for the selected hydrometric stations (located approximately between 25ºS to 40ºS; Figure 1c). Similar confidence in simulated runoff was illustrated by Beamer et al. (2016) when using SnowModel and HydroFlow for Gulf of Alaska drainage basins.

3. EOF analysis

We applied EOF analysis to characterize spatiotemporal pattern in runoff and water source. EOF is a tool that ordinates the spatial and temporal data to find combinations of locations that vary consistently through time and combinations of time that vary in a spatially consistent manner. More specifically, the first few major axes of the EOF analysis explain variations in river runoff through both time and space. Eigenvectors associated with such an analysis are linked to spatial locations and reveal the influence of different geographic locations on the summarized runoff patterns and allows further analyses of large-scale atmospheric-ocean covariates linked to the EOFs. In addition, the temporally summarized spatial data can be explored with cross-correlation analysis between the runoff patterns and larger scale atmospheric climate indices such as ENSO and PDO.

We applied EOF to total runoff (henceforth mentioned as runoff), rain-derived runoff, snowmelt-derived runoff, and ice melt-derived runoff (on Figure 4 the time series of simulated annual runoff anomaly from each individual drainage basin west of the continental divide for the period 1979–2014 is shown). Figure 5 provides a 'field' representation of the spatiotemporal pattern in basin annual runoff for rain, snow, ice, and the combined total, with latitude on the y-axis and time on the x-axis and colors indicating the spatiotemporal patterns. We specifically examined the eigenvectors of the first two EOFs (EOF1–2) to gain insight into the correlation between temporal trends and spatial locations. We also examined how the first two EOFs (temporal component) vary with two large-scale atmospheric-ocean indices: the multivariate ENSO Index obtained from Wolter and Timlin (2011) and the PDO obtained from Zhang et al. (1997). We used cross-correlation analyses for this, which allow insight into whether the runoff patterns are linked to ENSO and PDO as they occur or with a lag, where signals of ENSO or PDO show in the runoff patterns years after the events.

ENSO is comprised of different physical parameters observed across the tropical Pacific Ocean, such as sea-level pressure, surface air temperature, sea-surface temperature, cloud fraction, and the zonal and meridional components of the surface wind. Normalized positive ENSO values represent El Niño events and negative values La Niña events (Wolter and Timlin 2011). The PDO reflects climate variability in the Pacific Ocean, but over a longer time scale than the ENSO. The ENSO cycles typically remain in the same phase for 6–18 months, where the PDO may remain in the same phase for one to two decades. The PDO consists of cold (negative) and warm (positive) phases, defined by ocean sea-surface temperature anomalies in the northeast and tropical Pacific Ocean. These anomalies are implicated in upper level atmospheric winds causing droughts, and affect land-surface temperatures around the Pacific. When normalized sea-surface temperatures are anomalously cold for the central North Pacific and relatively warm near the equator and along the Pacific Coast of South America (and when standardized sea-level pressure is below average over the North Pacific), the PDO has a positive phase, and vice versa for the negative phase (e.g., Zhang et al. 1997). Importantly, if ENSO and PDO are in the same phase, impacts from El Niño and La Niña are likely reinforced, and vice versa when they are out of phase (e.g., Yuan and Martinson 2000, 2001).

4. Results and discussion

4.a Grid runoff distribution

SnowModel gridded 35-year (1979–2014) mean runoff and its rain-, snowmelt-, and ice melt-derived components for the Andes Cordillera west of the continental divide show highest runoff values for northern and southern parts of the domain (Figure 6a–d). Colombia and northern Ecuador (6°N–6°S), and Patagonia (38–45°S) estimates were greater than 5 m water

348 equivalent (w.e.). High values were expected for Patagonia, which is chronically impacted by
349 severe subpolar low-pressure systems and their attendant high precipitation rates (e.g., Romero
350 1985; Paruelo et al. 1998; Garreaud et al. 2009). The lowest runoff values (< 0.25 m w.e.) were
351 obtained along the coastal zone of Peru and between the Atacama Desert (18–20°S) and Santiago
352 de Chile (33°S), showing distinct regional-scale grid runoff variability throughout the simulation
353 domain.

354 For the domain, the simulated 35-year mean runoff was $136.5 \pm 12.2 \times 10^{10}$ m^3 (where ±
355 means one standard deviation; Table 2), distributed among Colombia ($40.9 \pm 5.6 \times 10^{10}$ m^3),
356 Ecuador ($21.0 \pm 5.6 \times 10^{10}$ m^3), Peru ($23.3 \pm 2.6 \times 10^{10}$ m^3), and Chile ($51.3 \pm 4.1 \times 10^{10}$ m^3)
357 (Table 2). This indicates that for the 35-year period, Colombia accounted for 30 %, Ecuador 15
358 %, Peru 17 %, and Chile 38 % of the domain's runoff (Table 2).

359 The gridded 35-year mean runoff correlates highly with the gridded 35-year mean rain
360 based runoff (Figure 6), where for the entire domain 86 %, or 116.9×10^{10} m^3, of the runoff
361 originated from rain (Table 2). This emphasizes that runoff, on average for the domain, is highly
362 influenced by a pluvial regime. In particular, the northern part of the domain was controlled by
363 rain-derived runoff, accounting for 99 % of the runoff from Colombia, Ecuador 97 %, Peru 86
364 %, and Chile 69 % (Table 2). Crespo et al. (2011) used observations to confirm this pluvial
365 regime for 13 monitored micro-basins in the Andes of southern Ecuador (4°S), where runoff was
366 strongly controlled by annual rainfall. Similar conclusions were stated by Rubio-Álvarez and
367 McPhee (2010) for southern Chile, where a decrease in runoff corresponded with decreasing
368 trends in observed precipitation. Therefore, along the Andes Cordillera the variability in runoff
369 was influenced by the meteorological conditions, including the north-south temperature gradient
370 – going towards relatively lower mean annual air temperatures in the south in Patagonia (sub-

371 polar climate), compared to the north (tropical climate) (Mernild et al. 2016a) – together with the
372 presence of increasing snow and glacier coverage toward Patagonia to the south.

373 Snowmelt-derived runoff (Figure 6c) over 35 years is spatially tied to snow duration in
374 the high Andes mountains and in Patagonia (for a detailed spatiotemporal description of snow
375 conditions in the Andes Cordillera, see Mernild et al. 2016a). Snowmelt runoff averaged <1 %
376 for Colombia, Ecuador (3 %), Peru (14 %), and Chile (24 %) (Table 2). For Chile, snowmelt
377 runoff contributions averaged higher than for any of the three countries within the domain
378 (Colombia, Ecuador, and Peru), emphasizing a higher degree of nival runoff, where the
379 maximum basin values of snow melt based runoff was ~60 % for central Chile and ~80 % for
380 Patagonia. Similar conditions are confirmed by e.g., Masiokas et al. (2006), Favier et al. (2009),
381 Melo et al. (2010), and Mernild et al. (2016b), where snowpack and snowmelt changes on the
382 individual basin-scale in central Chile, central-western Argentina, and Norte Chico region was
383 the primary source for runoff, annual variability, and water budget.

384 Ice melt-derived runoff (Figure 6d) is scattered along the Andes Cordillera. The ratio
385 between ice melt base runoff and runoff is <1 % for Colombia, Ecuador, and Peru and 7 % for
386 Chile (Table 2), associated with the increasing ice coverage toward the south. Due to ongoing
387 temporal changes in ice coverage for South America, where glaciers have retreated and thinned
388 in response to climate changes since the end of the Little Ice Age (e.g., Masiokas et al. 2006; Le
389 Quesne et al. 2009; Malmros et al. 2016), it is expected that the ratio between ice melt-derived
390 runoff and total runoff will decrease because the annual ice melt-derived runoff will decline as
391 reductions in glacier area outweigh the effect of glacier melting (AMAP 2011).

392 Overall, for the domain, 95 % of the simulated runoff originated from non-glacierized
393 basins and 5 % from glacierized basins (Table 2), highlighting that rain-derived runoff from non-

glacierized basins is the greatest contributor to runoff west of the continental watershed divide. For the 35-year period, Colombia, Ecuador, and Peru, >99 % of the river runoff was from non-glacierized basins, and <1 % was from glacierized basins; for Chile, it was 87 % and 13 %, respectively (Table 2). On pentadal scales (1979/80–1983/84, 1984/85–1988/89, etc.), the ratios between simulated mean runoff from non-glacierized and glacierized areas are not significantly different compared to the mean ratio for the 35-year period. The same insignificant differences in ratios occurred between runoff and rain, runoff and snowmelt, and runoff and ice melt between pentadal mean values and the 35-year mean value, even though runoff for the domain changed by 0.94×10^{10} m^3 yr^{-1} (significant; $p < 0.01$) for the simulation period (Table 2). When analyzed by specific countries, runoff changed by 0.43×10^{10} m^3 yr^{-1} for Ecuador (significant; $p < 0.01$), 0.37×10^{10} m^3 yr^{-1} for Colombia (significant; $p < 0.01$), 0.17×10^{10} m^3 yr^{-1} for Chile (insignificant), and 0.03×10^{10} m^3 yr^{-1} for Peru (insignificant) over the 35-year period (Table 2).

4.b Spatial distribution of basin runoff

In Figures 7 and 8, SnowModel-simulated 35-year mean river runoff is shown together with runoff trends from each individual drainage basin outlet west of the continental divide. The figures include rain-derived runoff, snowmelt-derived runoff, and ice melt-derived runoff, runoff from non-glacierized areas, glacierized areas, and specific runoff (runoff volume per unit drainage area per time, L s^{-1} km^{-2}). In Figures 7a–f, variability in the 35-year mean runoff between neighboring basins occurred (these runoff variations are expected to be useful for future studies linking these runoff to coastal circulations to understand the linkages between terrestrial and marine environments). It is reasonable to believe that the differences in mean basin runoff regimes between pluvial, nival, and glacionival are related to geographical locations and

differences in basin characteristics (e.g., size and hypsometry), snow coverage, ice coverage, and climate forcing functions. For example, the Andes Cordillera acts as a topographic barrier enhancing the terrestrial precipitation on the western sides (e.g., Mernild et al. 2016a), contributing to the pluvial regimen in river runoff. High 35-year mean basin river outlet runoff (maximum: $7.3 \pm 1.9 \times 10^{10}$ m^3; 2°S) and high linear runoff trends (maximum: 0.2×10^{10} m^3 yr^{-1}; 2°N) occurred in the northern part of the domain in Colombia and Ecuador and in the lower half of the domain, especially around the Lake District of Chile (39–41°S) (Figures 7a and 8a) (linear spatial runoff trends (Figure 8) which are not significantly different from the normalized spatial runoff trends are not shown). The simulated runoff distribution for the southern part of Chile (35–55°S) is in accordance with Dávila et al. (2002), who found the highest freshwater input through rivers to the South Eastern Pacific Ocean occurred during the period 1951–1980. In Colombia and Ecuador, river runoff is dominated by tropical climate conditions and rain (Figure 9a). Basins where river runoff is dominated by rain (pluvial regimes) cluster north of 40°S (Figure 9a). South of 40°S, including the area around the Lake District, river runoff originated from all three components (Figure 9a), and was highly dependent on the distribution of non-glacierized and glacierized basins combined with the presence and variability in snow and glacier coverage (Figure 9b), basin area and hypsometry, and climate conditions. In Chile, the relative rain contribution to river runoff is lower while snow and ice melt contributions are higher than any of the other three countries Colombia, Ecuador, and Peru (Table 2).

On an individual basin scale, in central Chile and central-western Argentina, runoff originated from snowmelt. This is in line with Masiokas et al. (2006) and Melo et al. (2010), where snowmelt is the primary source for river runoff. In the Chilean Lake District, however, the Andes Cordillera drops in elevation, and runoff originated mainly from rain (from the rainy

climate conditions with Mediterranean influences (information based on, e.g., meteorological observations operated by the Dirección Meteorológica de Chile; Mernild et al. 2016a)), and during the Austral winter season (June–August) (for more about the seasonal variability in runoff, see further below). Further, around the Chilean Lake District (37.5–40°S) the simulated runoff trends (1979–2014) from each individual drainage basin outlet (n = 75) was, on average, slightly increasing (insignificant), where observed runoff trends (1952–2003) from selected basins (n = 25), on average, were decreasing (significant) (Rubio-Álvarez and McPhee 2010); this is consistent with decreasing trends in observed precipitation. However, a direct comparison is not possible due to the differences in time periods between the simulations and streamflow records.

Regarding the lowest 35-year mean basin runoff around the arid Atacama Desert (minimum: $7.0 \pm 5.6 \times 10^4$ m^3; 22°S) no linear change in runoff trends occurred (Figures 8a–f). This is a region where the annual precipitation typically is <0.25 m w.e. (e.g., Mernild et al., 2016a) and runoff from snowmelt and ice melt is negligible.

When analyzing the SnowModel simulated basin specific runoff, the 35-year mean specific runoff and the linear trends in specific runoff both show a characteristic pattern – an hourglass shape – for the Andes Cordillera west of the continental divide (Figures 7g and 8g). Specific runoff patterns are even more pronounced toward the hourglass shape than the runoff patterns (mean and trend patterns) displayed in Figures 7a and 8a. The 35-year mean simulated specific runoff show that annual maximum specific runoff (>100 L s^{-1} km^{-2}) are present in the northern and the southern parts of the domain, and that annual minimum specific runoff (<10 L s^{-1} km^{-2}) occurs in the area around the arid Atacama Desert and south toward Santiago (Figure 7g). SnowModel simulations of specific runoff are in qualitative agreement with specific runoff

values estimated by Cortés et al. (2011) obtained from several rivers on the western slopes of the central and southern Chilean Andes Cordillera (30–40°S; 1961–2006), spanning from ~8 L s^{-1} km^{-2} (for the Arrayan en la Montosa basin; 33.33°S) to ~65 L s^{-1} km^{-2} (for Claro en los Queñes basin; 34.98°S). A direct comparison is, however, not possible due to the differences in time periods between simulations and streamflow records. Regarding linear changes in specific runoff, the greatest changes were seen both in the north and the south of the domain (>1 L s^{-1} km^{-2} yr^{-1}), and lowest changes in the center part of the domain from the arid Atacama Desert to the area around Santiago (<0.5 L s^{-1} km^{-2} yr^{-1}) (Figure 8g).

Figure 10a illustrates SnowModel-simulated runoff, rain-derived runoff, snowmelt-derived runoff, ice melt-derived runoff, runoff from non-glacierized basins, and glacierized basins along the Andes Cordillera for all seasons: winter (June–August), spring (September–November), summer (December–February), and autumn (March–May). Along the Andes Cordillera the seasonal distribution in river runoff (here expressed in relative values) dominates in summer and autumn between 8°N–8°S (where up to ~40 % of the annual basin runoff occur both during summer and autumn for specific basins), in summer between 8–23°S and 45–57°S (where up to ~60 % of the annual basin runoff occur for specific basins), and in winter between 23–45°S (where up to ~60 % of the annual runoff occur for specific basins) (Figure 10a). This indicates a seasonal variability in runoff along the Andes Cordillera.

In addition to the seasonal variability in runoff along the Andes Cordillera, the amount of summer runoff seems to be in "systematic" anti-phase with the amount of winter runoff (here expressed in relative values) (Figure 10a). Along the Andes Cordillera the amount of relative winter basin river runoff indicates an 'S-shaped' profile, while in contrast the amount of relative summer runoff indicates an inverse 'S-shaped' profile. During spring and autumn, the variability

in runoff is less pronounced along the Andes Cordillera compared to summer and winter where seasonal variability in runoff around Atacama Desert is insignificantly different. Here, each season counts for around one-quarter of the annual runoff, indicating no seasonal variability in simulated river runoff over the 35 year period (Figure 10a). Since rain dominates the runoff pattern for the domain, the rain-derived runoff distribution (Figure 10b) and the runoff non-glacierized basin distribution (Figure 10e) are similar to the overall seasonal runoff pattern, at least north of 40°S (Figure 10a). South of 40°S, runoff is dominant in winter, spring, and summer (Figures 10c and 10d), and originates from snow and ice melt and from glacierized basins (Figure 10e and 10f).

4.c EOF river runoff variance analysis

The EOF analysis (Figures 11–13) suggests that the SnowModel simulated annual basin river runoff dataset can be summarized by two major axes (modes: EOF1 and EOF2) for runoff, rain-derived runoff, snowmelt-derived runoff, and ice melt-derived runoff (Figure 11). Several assessments of significance associated with each mode (EOF; see https://github.com/marchtaylor/sinkr), implementation of North's rule and two bootstrapping methods indicate that EOF1, EOF2, and EOF3 are significant. EOF1 explains 46 %, 44 %, 41 %, and 42 % of the explained variance in total, rain-, snow-, and ice-derived river runoff, respectively. EOF2's explained variance is lower than EOF1 for the same variables: 16%, 16%, 14%, and 13%.

In Figure 11, we provide the temporal EOF1 and the 5-year running mean smooth total for runoff and its constituents. Smoothing lines reveal a pattern of positive values for the first ~20 years of the simulation period (1979–1999) followed by negative values (2000–2014). When

EOF1 is positive, runoff is relatively low and vice versa, meaning that overall the freshwater river runoff and rain-derived runoff increase (Figure 11; Table 2). This increase in runoff was most pronounced for the last ~15 years (2000–2014) (Figure 11), and less for the first ~20 years. EOF1 thus indicates a temporal increase in both runoff parameters for the domain (Figure 11).

The temporal cycle of EOF patterns has associated spatial elements, derived from the eigenvectors (Figure 12). These eigenvectors reveal the spatial pattern in the correlation between the temporal trends captured by the EOFs and each individual basin along the Andes Cordillera (Figure 12). Overall, the temporal trend in EOF1 are shared by nearly all basins north of 30°S (as indicated by the negative correlation), and only by specific basins (or regions) south of 30°S. This indicates a geographic separation – a distinct out-of-phase variation in runoff time series in comparison to the overall domain for the last 35 years (Figures 12a and 12b). Snowmelt-derived runoff and ice melt-derived runoff are more diverse (Figures 12c and 12d) than total runoff and rain-derived runoff. We conclude that the differences in runoff patterns (including rain-derived runoff, snowmelt-derived runoff and ice melt-derived runoff) shown for the Andes Cordillera west of the continental divide are due partly to specific basin characteristics (e.g., size, aspect, elevation range, hypsometry, length of the routing network, and glacier cover), and partly due to different climate forcing functions (e.g., air temperature and precipitation) that are influenced by large-scale modes of Pacific Ocean natural variability such as ENSO and PDO (see below; Rosenblüth et al. 1997; Schneider and Gies 2004; Garreaud 2009; Garreaud et al. 2009). This is confirmed for Colombia, since the SnowModel MERRA simulations were able to reproduce the observed link between inter-annual variabilities in river runoff and ENSO (not shown) as reported by Poveda et al. (2001).

We also detected a pattern associated with EOF2. EOF2 has a temporal component that is roughly opposite of the temporal EOF1 pattern especially for runoff and rain-derived runoff (see Figure 11), though both patterns show approximately the same frequency. The EOF2 5-years running mean smoothing lines for runoff and rain-derived runoff are shown to be negative for the first ~15 years (1979–1994) and hereafter positive (Figure 11). The importance of this second pattern is in the spatial correlations of EOF2. This additional pattern is associated with a different geographic breakdown where runoff north of the Atacama Desert is negatively correlated with basin runoff located to the south; substantial basin and regional variations in annual runoff time series for South America have occurred since 1993 (Figure 12, second row). Due to the existence of these variability patterns for EOF1 and EOF2, we suggest that variations in basin runoff along the Andes Cordillera overall can be divided into two regions (north and south of 20–30°S), even though runoff variability for some basins within both regions will be different.

We gained further insight into the source of EOF1 and EOF 2 temporal patterns (Figure 13) via cross-correlation analysis between the EOFs and ENSO or PDO. Overall, we detected a strong immediate effect of both PDO and ENSO. In Figure 13, positive correlations between EOF1 and PDO ($r = 0.31$; significant, $p < 0.01$), and between EOF1 and ENSO ($r = 0.32$; significant, $p < 0.01$), runoff ($r = 0.31$; significant, $p < 0.01$) and rain-derived runoff ($r = 0.32$; significant, $p < 0.01$) are seen at a zero-lag. There is a real-time covariation between the pattern in EOF1 and changes in PDO and ENSO occurred. This supports the findings by Poveda et al. (2001), who proposed that a large-scale natural variability in ENSO is closely related to river runoff variations in Colombia.

Regarding rain-derived runoff, when both PDO and ENSO are strong, EOF1 is positive and runoff is low. Regarding snowmelt-derived runoff, it appears to be lagging behind PDO ($r =$

554 0.60; significant, $p < 0.01$) and ENSO ($r = 0.32$; significant, $p < 0.05$) by 1-2 years – the cause of
555 the delay from PDO seems clear, since ENSO cycles typically remain in the same phase for 6–18
556 months, whereas PDO can remain in the same phase for one–two decades (Mernild et al. 2015).
557 A similar delay is observed for ice melt-derived runoff ($r = -0.61$ and $r = -0.46$; both significant
558 and both $p < 0.01$) (Figure 13). For snowmelt-derived runoff, when both PDO and ENSO are
559 strong and positive, EOF1 is positive, meaning a decrease in snowmelt-derived runoff. In
560 contrast, for ice melt-derived runoff when both PDO and ENSO are strong and positive, EOF1 is
561 negative, meaning an increase in ice melt-derived runoff. One to two years after strong PDO and
562 ENSO years with reduced rain-derived runoff, it is likely that increasing ice melt-derived runoff
563 and decreasing snowmelt-derived runoff will prevail. Overall, if the end-of winter snowpack is
564 relatively low, the start of the ablation of the underlying ice will start relative early, likely
565 indicating a relatively low snowmelt-derived runoff and a high ice-melt-derived runoff.
566
567 *4.d Perspectives and knowledge gaps*

568 To continue the work of understanding the links among changing climate and cryosphere
569 and hydrosphere changes, more extensive and accurate records of the spatiotemporal river runoff
570 for the Andes Cordillera are required to examine the links between atmosphere, terrestrial, and
571 oceanic (hydrographic) conditions, and the potential impacts on Earth's climate system. For
572 example, simulated runoff can be used as input in dynamic ocean models. In the Andes
573 Cordillera and worldwide, present and projected future snow cover diminishing and glacier
574 mass-balance loss and retreat (e.g., Liston and Hiemstra 2011; Marzeion et al. 2012; Gardner et
575 al. 2013; Mernild et al. 2013, 2016a; Radić et al. 2013; WGMS 2014) raise concern about the
576 sustainability of drinking water and irrigation supplies and hydropower production (highly

577 relevant for glacierized basins). Future hydrological changes will likely have social health and
578 socioeconomic implications. However, in the Andes Cordillera the majority of the river runoff
579 regimes are pluvially controlled, emphasizing a potential effect on freshwater water resource
580 availability due to future projected changes in climate.

581 This series of SnowModel papers (Parts I–IV; Mernild et al. 2016a, 2016b, 2016c) has
582 linked the conditions in the atmosphere with cryospheric and hydrological conditions in the
583 Andes Cordillera to understand the hydrological cycle influenced by changes in precipitation,
584 snow cover, and glacier mass-balance. Even though SnowModel is a sophisticated model, more
585 research is still needed. For instance, in the Andes Cordillera there is still a knowledge gap
586 regarding changes in terrestrial hydrological processes and their implications on
587 geomorphological processes, biogeochemical weathering and nutrient fluxes, aquatic
588 ecosystems, vegetation changes, and human interventions. By doing so, we will improve our
589 understanding of the key socioeconomic consequences of changes to the freshwater system, but
590 we will also be able to assess the present and future potential for parts of the Andes Cordillera to
591 become sources of freshwater for water-poor regions, such as in the Santiago de Chile and
592 Atacama regions, where mining activities are heavily dependent on water.

593

594 **5. Conclusions**

595 A merging of SnowModel (a spatially-distributed meteorological, full surface energy
596 balance, snow and ice evolution model) and HydroFlow (a linear-reservoir runoff routing model)
597 with NASA MERRA atmospheric forcing data was used to simulate hydrological conditions for
598 the Andes Cordillera (west of the continental divide). The analysis included freshwater river
599 runoff, runoff routing, and the spatiotemporal distribution of basin outlet river runoff to the

surrounding fjords and seas for the 35-year period 1979 through 2014. Simulated river runoff time series were verified against DGA observed runoff time series (from the central part of Chile), showing agreement between simulations and observations.

The 35-year mean (1979–2014) gridded runoff varied considerably over distances, varying from high runoff in Colombia, Ecuador, and Patagonia to low runoff along the coastline of Peru and between the Atacama Desert and Santiago de Chile. On average, 86 % of the total runoff from the Andes Cordillera originated from rain-derived runoff, indicating, on average, a pluvial river regime. In Colombia and Chile the proportions of rain-derived runoff were 99 % and 69 %, respectively. Overall, 95 % of the simulated runoff originated from non-glacierized basins. Over the 35-year period, runoff changed significantly (0.94×10^{10} m^3 yr^{-1}; $p < 0.01$), with the largest increases occurring in Ecuador and Colombia, whereas the increases in runoff were insignificant in Chile and Peru.

The spatial distribution of runoff from each individual drainage basin showed a 35-year mean range in basin runoff from $7.0 \pm 5.6 \times 10^{10}$ m^3 (22°S) to $7.3 \pm 1.9 \times 10^{10}$ m^3 (2°S), where the specific runoff pattern showed a characteristic *hourglass shape* for the Andes Cordillera with specific runoff values >100 L s^{-1} km^{-2} for the northern and southern parts of the Andes Cordillera, and <10 L s^{-1} km^{-2} around the arid Atacama Desert. Further, a distribution of basin runoff into rain-derived runoff, snowmelt-derived runoff, and ice melt-derived runoff emphasized that basins dominated by rain-derived runoff were primarily located north of 40°S, and that south of 40°S basin river runoff originated from all three components.

Mapping and understanding the spatiotemporal river runoff conditions for the Andes Cordillera (west of the continental divide) are of interest for our understanding of a changing climate and changes in the cryosphere and hydrosphere (as described in these SnowModel Parts

623 I–IV papers; Mernild et al. 2016a, 2016b, 2016c). Models of hydrological conditions and
624 variability are important for understanding key socioeconomic consequences of changes to the
625 freshwater system and freshwater conditions as a source for water-poor regions.

626

627 **Acknowledgements**

628 We thank the anonymous reviewers for their valuable reviews and their insightful critique of this
629 article. This work was supported by the National Science Foundation of Chile *Fondecyt* under
630 Grant Agreement #1140172. All model data requests should be addressed to the first author. We
631 thank Direction General de Aguas for providing observed river runoff time series from Chile.
632 The authors have no conflict of interest.

633

634

635

636

637

638

639

640

641

642

643

644

645

References

Ayala, A., McPhee, J., and Vargas, X. 2014. Altitudinal gradients, midwinter melt, and wind effects on snow accumulation in semiarid mid-latitude Andes under La Niña conditions. *Water Resour. Res.*, 50, 3589–3594, doi:10.1002/2013WR01496.

AMAP 2011. Snow, Water, Ice and Permafrost in the Arctic (SWIPA): Climate Change and the Cryosphere. Chapter 7: Mountain Glaciers and Ice Caps, 61 pp. Arctic Monitoring and Assessment Program (AMAP), Oslo, Norway, xii + 538 pp.

Baraer, M., Mark, B., McKenzie, J., Condom, T., Bury, J., Huh, K.-I., Portocarrero, C., Gomez, J. and Rathay, S. 2012. Glacier recession and water resources in Peru's Cordillera Blanca, *Journal of Glaciology*, 58(207), 134–150, doi:10.3189/2012JoG11J186.

Beamer, J. P., Hill, D. F., Arendt, A., and Liston, G. E. 2016, High-resolution modeling of coastal freshwater discharge and glacier mass balance in the Gulf of Alaska watershed. *Water Resour. Res.*, 52, 3888–3909, doi:10.1002/2015WR018457.

Bing, A., Fedorova, I., Dibike, Y., Karlsson, J. M., Mernild, S. H., Prowse, T., Semenova, O., Stuefer, S., and Woo, M.-K. 2016. Arctic terrestrial hydrology: A synthesis of processes, regional effects and research challenges. *Journal of Geophysical Research*, doi: 10.1002/2015JG003131.

Bliss, A., Hock, R., and Radić, V. 2014. Global response of glacier runoff to twenty-first century climate change, *J. Geophys. Res. Earth Surf.*, 119, doi:10.1002/2013JF002931.

Bosilovich, M. G., 2008. NASA's Modern Era Retrospective Analysis for Research and Applications: Integrating Earth observations. *Earthzine*. [Available online at http://www.earthzine.org/2008/09/26/nasas-modern-era-retrospective-analysis/.]

675 Bosilovich, M. G., Chen, J., Robertson, F. R., and Adler, R. F. 2008. Evaluation of global
676 precipitation re-analyses. *J. Appl. Meteor. Climatol.*,47, 2279–2299,
677 doi:10.1175/2008JAMC1921.1.
678
679 Bosilovich, M. G., Franklin, R. R., and Chen, J. 2011. Global energy and water budgets in
680 MERRA. *Journal of Climate*, 24, 5721–5739, doi:10.1175/2011JCLI4175.1.
681
682 Carrasco, J. F., Casassa, G., and Quintana, J. 2005. Changes of the 0°C isotherm and the
683 equilibrium line altitude in the central Chile during the last quarter of the 20th century. *Hydrol.*
684 *Sci. — J. Sci. Hydrol.*, 50(6), 933–948, doi.org/10.1623/hysj.2005.50.6.933.
685
686 Cornwell, E., Molotch, N. P., and McPhee, J. 2016. Spatio-temporal variability of snow water
687 equivalent in the extra-tropical Andes Cordillera from distributed energy balance modeling and
688 remotely sensed snow cover. *Hydrol. Earth Syst. Sci.*, 20, 411-430, doi:10.5194/hess-20-411-
689 2016.
690
691 Cortés, G., Vargas, X., and McPhee, J. 2011. Climatic sensitivity of streamflow timing in the
692 extratropical western Andes Cordillera. *Journal of Hydrology*, 405(1), 93–109.
693
694 Crespo, P. , Feyen, J. , Buytaert, W. , Bücker, A. , Breuer, L. , Frede, H. G. and Ramírez, M.
695 2011. Identifying controls of the rainfall–runoff response of small catchments in the tropical
696 Andes (Ecuador), *Journal of Hydrology*, 407 (1-4), pp. 164-174 . doi:
697 10.1016/j.jhydrol.2011.07.021.
698
699 Cortés, G., Vargas, X., and McPhee, J. 2011. Climatic sensitivity of streamflow timing in the
700 extratropical western Andes Cordillera, *Journal of Hydrology*, 405 (1), 93-109.
701
702 Cullather, R. I., and Bosilovich, M. G. 2011. The moisture budget of the polar atmosphere in
703 MERRA. *Journal of Climate*, 24, 2861–2879, doi:10.1175/2010JCLI4090.1.
704

Danielson, J. J. and Gesch, D. B. 2011. Global multi-resolution terrain elevation data 2010 (GMTED2010). U.S. Geological Survey Open-File Report 2011–1073, 26 p.

Dávila, P. M., Figueroa, D., and Uller, E. M. 2002. Freshwater input into the coastal ocean and its relation with the salinity distribution offaustral Chile (35–55°S). *Continental Shelf Research*, 22(3), 521–534.

Escobar, F., Casassa, G., and Pozo, V. 1995. Variaciones de un glaciar deMontaña en los Andes de Chile Central en las últimas dos décadas. *Bull. Inst. Fr. Etudes Andines* (Lima), 24(3), 683–695.

Favier, V., Falvey, M., Rabatel, A., Praderio, E. and López, D. 2009. Interpreting discrepancies between discharge and precipitation in high-altitude area of Chile's Norte Chico region (26–32°S), *Water Resour. Res.,* 45(2), W02424, doi:10.1029/2008WR006802.

Fleischbein, K., Wilcke, W., Valarezo, C., Zech, W. and Knoblich, K. 2006. Water budgets of three small catchments under montane forest in Ecuador: experimental and modelling approach. *Hydrological Processes*, 20(12), 2491–2507.

Gardner, A.S., Moholdt, G., Cogley, J. G., Wouters, B., Arendt, A. A., Wahr, J., Berthier, E., Hock, R., Pfeffer, W. T., Kaser, G., Ligtenberg, S. R. M., Bolch, T., Sharp, M. J., Hagen, J. O., van den Broeke, M., and Paul, F. 2013. A Reconciled Estimate of Glacier Contribution to Sea Level Rise: 2003 to 2009. *Science*, 340, 852–857.

Garreaud, R. D. 2009. The Andes climate and weather. *Adv. Geosci.*, 7, 1–9.

Garreaud, R.D., Vuille, M., Compagnucci, R., Marengo, J., 2009. Present-day South American climate. *Palaeogeogr. Palaeoclimatol. Palaeoecol*., 281 (3–4), 180–195.

734 Gascoin, S., Kinnard, C., Ponce, R., Macdonell, S., Lhermitte, S. and Rabatel, A. 2011. Glacier
735 contribution to streamflow in two headwaters of the Huasco River, Dry Andes of Chile. *The*
736 *Cryosphere*, (5), 1099–1113.
737
738 Gordon, R. P., Lautz, L. K., McKenzie, J. M., Mark, B. G., Chavez, D. and Baraer, M. 2015.
739 Sources and pathways of stream generation in tropical proglacial valleys of the Cordillera
740 Blanca, Peru. *Journal of Hydrology*, 522, 628–644, doi:10.1016/j.jhydrol.2015.01.013.
741
742 Hall, D. K., Riggs, G. A., and Salomonson, V. V. 1995. Development of methods for mapping global
743 snow cover using Moderate Resolution Imaging Spectroradiometer (MODIS) data. *Remote Sensing*
744 *of Environment*, 54, 127– 140.
745
746 Hall, D. K., Salomonson, V. V., and Riggs, G. A. 2006. MODIS/Terra Snow Cover Daily L3 Global
747 500m Grid. Version 5. Fractal snow cover. Boulder, Colorado USA: NASA National Snow and Ice
748 Data Center Distributed Active Archive Center.
749
750 Hall, D. K. and Riggs, G. A. 2007. Accuracy assessment of the MODIS snow products. *Hydrological*
751 *Processes,* 21, 1534–1547, doi:10.1002/hyp.6715.
752
753 Hock, R., Jansson, P., and Braun, L. 2005. Modelling the response of mountain glacier discharge
754 to climate warming, in Global Change and Mountain Regions—A State of Knowledge
755 Overview, edited by U.M. Huber, M. A. Reasoner, and H. Bugmann, pp. 243–252, Springer,
756 Dordrecht.
757
758 Jansson, P., Hock, R. and Schneider, T. 2003. The concept of glacier water storage—A review.
759 *Journal of Hydrology*, 282(1–4), 116–129, doi:10.1016/S0022-1694(03)00258-0.
760
761 Le Quesne, C., Acuna, C., Boninsegna, J. A., Rivera, A. and Barichivich, J. 2009. Long-term
762 glacier variations in the Central Andes of Argentina and Chile, inferred from historical records
763 and tree-ring reconstructed precipitation. *Palaeogeography Palaeoclimatology Palaeoecology*,
764 281(3-4), 334-344.
765

766 Liston, G. E. 1995. Local advection of momentum, heat, and moisture during the melt of patchy
767 snow covers. *Journal of Applied Meteorology*, 34, 1705–1715, doi:10.1175/1520-0450-
768 34.7.1705.
769
770 Liston, G. E. and Elder, K. 2006b. A distributed snow-evolution modeling system (SnowModel).
771 *Journal of Hydrometeorology*, 7, 1259–1276, doi:10.1175/JHM548.1.
772
773 Liston, G. E. and Elder, K. 2006a. A meteorological distribution system for high-resolution
774 terrestrial modeling (MicroMet). *Journal of Hydrometeorology*, 7, 217–234,
775 doi:10.1175/JHM486.1.
776
777 Liston, G. E., Haehnel, R. B., Sturm, M., Hiemstra, C. A., Berezovskaya, S., and Tabler, R. D.
778 2007. Simulating complex snow distributions in windy environments using SnowTran-3D.
779 *Journal of Glaciology*, 53, 241–256.
780
781 Liston, G. E. and Hiemstra, C. A. 2011.The Changing Cryosphere: Pan-Arctic Snow Trends
782 (1979–2009). *Journal of Climate*, 24, 5691–5712.
783
784 Liston, G. E. and Mernild, S. H. 2012. Greenland freshwater runoff. Part I: A runoff routing
785 model for glaciated and non-glaciated landscapes (HydroFlow). *Journal of Climate,* 25(17),
786 5997–6014.
787
788 Liston, G. E., and Sturm, M. 1998. A snow-transport model for complex terrain. *Journal of*
789 *Glaciology*, 44, 498–516.
790
791 Liston, G. E., and Sturm, M. 2002. Winter precipitation patterns in Arctic Alaska determined
792 from a blowing-snow model and snow depth observations. *Journal of Hydrometeorology*, 3,
793 646–659.
794

Liston, G. E., Winther, J.-G., Bruland, O., Elvehøy, H., and Sand, K. 1999. Below surface ice melt on the coastal Antarctic ice sheet. *Journal of Glaciology*, 45, 273–285, doi:10.3189/002214399793377130.

López-Moreno, J. I., Fontaneda, S., Bazo, J., Revuelto, J., Azorin-Molina, C., Valero-Garcés, B., Morán-Tejeda, E., Vicente-Serrano, S. M., Zubieta, R., Alejo-Cochachín, J. 2014. Recent glacier retreat and climate trends in Cordillera Huaytapallana, Peru. Global Planetary Change, 112, 1–11.

Malmros, J. K., Mernild, S. H., Wilson, R., Fensholt, R., and Yde, J. C. 2016. Glacier changes in the Rio Olivares catchment, central Chilean Andes, 1955–2013. *Journal of Glaciology*, 62(232), 391–401, doi: 10.1017/jog.2016.43.

Masiokas, M.H., Villalba, R., Luckman, B., LeQuesne, C., Aravena, J.C., 2006. Snowpack variations in the central Andes of Argentina and Chile, 1951–2005: large-scale atmospheric influences and implications for water resources in the region. *Journal of Climate*, 19 (24), 6334–6352.

Masiokas, M.H., Villalba, R., Luckman, B. H., Le Quesne, C., and Aravena, J. C. 2006. Snowpack variations in the central Andes of Argentina and Chile, 1951–2005: Large-scale atmospheric influences and implications for water resources in the region. *Journal of Climate*, 19(24), 6334–6352.

McClung, D.M. 2013. The effects of El Niño and La Niña on snow and avalanche patterns in British Columbia, Canada, and central Chile. *Journal of Glaciology*, 59(216), 783–792.

Melo, O., Vargas, X., Vicuna, S., Meza, F., and McPhee, J. 2010. Climate Change Economic Impacts on Supply of Water for the M & I Sector in the Metropolitan Region of Chile. *Watershed Management*, 159–170, doi: 10.1061/41143(394)15.

825 Mernild, S. H. 2006. The internal drainage system of the lower Mittivakkat Glacier, Ammassalik
826 Island, SE Greenland. *Danish Journal of Geography*, 106, 13–24.
827
828 Mernild, S. H., Hasholt, B. and Liston, G. E. 2006. Water flow through Mittivakkat Glacier,
829 Ammassalik Island, SE Greenland. *Danish Journal of Geography*, 106, 25–43.
830
831 Mernild, S. H., Beckerman, A. P., Yde, J. C., Hanna, E., Malmros, J. K., Wilson, R., and Zemp,
832 M. 2015. Mass loss and imbalance of glaciers along the Andes to the sub-Antarctic islands.
833 *Global and Planeratary Change*, 1–11, 10.1016/j.gloplacha.2015.08.009.
834
835 Mernild, S. H. and Liston, G. E. 2012. Greenland freshwater runoff. Part II: Distribution and
836 trends, 1960–2010. *Journal of Climate,* 25(17), 6015–6035.
837
838 Mernild, S. H., Liston, G. E., and Hiemstra, C. A. 2014. Northern Hemisphere glaciers and ice
839 caps surface mass balance and contribution to sea-level rise. *Journal of Climate*, 27(15), 6051–
840 6073, doi.org/10.1175/JCLI-D-13-00669.1.
841
842 Mernild, S. H., Liston, G. E., Hiemstra, C. A., Malmros, J. K., and McPhee, J. 2016a. The Andes
843 Cordillera. Part I: Snow Distribution, Properties, and Trends (1979–2014). *International Journal*
844 *of Climatol*ogy, 1–19, doi: 10.1002/joc.4804.
845
846 Mernild, S. H., Liston, G. E., Hiemstra, C. A., Yde, J. C., McPhee, J., and Malmros, J. K. 2016b.
847 The Andes Cordillera. Part II: Rio Olivares Basin Snow Conditions (1979–2014), Central Chile.
848 *International Journal of Climatology*, 1–17, doi:10.1002/joc.4828.
849
850 Mernild, S. H., Liston, G. E., Hiemstra, C. A., and Wilson, R. 2016c. The Andes Cordillera. Part
851 III: Glacier Surface Mass Balance and Contribution to Sea Level Rise (1979–2014). In review
852 *International Journal of Climatology,* 1–21*,* doi: 10.1002/joc.4907.
853
854 Montecinos, A. and Aceituno, P. 2002. Seasonality of the ENSO-related rainfall variability in
855 central Chile and associated circulation anomalies. *Journal of Climate*, 16, 281–296.

Nash, J. E., and Sutcliffe, J. V. 1970. River flow forecasting through conceptual models, Part I – A discussion of principles. *Journal of Hydrology*, 10, 282–290.

North, G. R., Bell, T. L., Cahalan, R. F., and Moeng, F. J. 1982. Sampling errors in the estimation of empirical orthogonal functions. *Mon. Weather Rev*. 110, 699–706.

Paruelo, J. M., Beltran, A., Jobbagy, E., Sala, O. E., Golluscio, R. A. 1998. The Climate of Patagonia: general patterns and controls on biotic processes. *Ecologia Austral*, 8, 85–101.

Pfeffer, W. T., Arendt, A. A., Bliss, A., Bolch, T., Cogley, J. G., Gardner, A. S., Hagen, J.-O., Hock, R., Kaser, G., Kienholz, C., Miles, E. S., Moholdt, G., Molg, N., Paul, F., Radić, V., Rastner, P., Raup, B. H., Rich, J., Sharp, M. J., and The Randolph Consortium. 2014. The Randolph Glacier Inventory: a globally complete inventory of glaciers. *Journal of Glaciology*, 60(221), 537–552.

Poveda, G., Jaramillo, A., Gil, M. M., Quiceno, N., and Mantilla, R. I. 2001. Seasonally in ENSO-related precipitation, river discharges, soil moisture, and vegetation index in Colombia, *Water Resources Research*, 37(8), 2169–2178.

Preisendorfer, R.W. 1998. Principal Component Analysis in Meteorology and Oceanography. In: Mobley, C.D. (Ed.) Elsevier, Amsterdam, p. 452.

Rienecker, M. M., and Coauthors, 2011: MERRA: NASA's Modern-Era Retrospective Analysis for Research and Applications. *Journal of Climate*, 24, 3624–3648, doi:10.1175/JCLI-D-11-00015.1.

Romero, H., 1985. Geografıa de los Climas. Geografıa de Chile. Instituto Geografico Militar. Tomo XI, 243pp.

886 Robertson, F. R., M. G. Bosilovich, J. Chen, and T. L. Miller, 2011: The effect of satellite
887 observing system changes on MERRA water and energy fluxes. *Journal of Climate*, 24, 5197–
888 5217, doi:10.1175/2011JCLI4227.1.
889
890 Rosenblüth, B., Fuenzalida, H.A., Aceituno, P., 1997. Recent temperature variations in Southern
891 South America. *Int. J. Climatol.*, 17, 67–85.
892
893 Rubio-Álvarez, E., and McPhee, J. 2010. Patterns of spatial and temporal variability in
894 streamflow records in south central Chile in the period 1952–2003. *Water Resources Research*,
895 46(5), W05514, doi:10.1029/2009WR007982.
896
897 Rutllant, J., and Fuenzalida, H. 1991. Synoptic aspects of the central Chile rainfall variability
898 associated with the southern oscillation. *International Journal of Climatology*, 11(1), 63–76.
899
900 Sagredo, E.A., and Lowell, T.V. 2012. Climatology of Andean glaciers: a framework to
901 understand glacier response to climate change. *Glob. Planet. Chang.*, 86–87, 101–109.
902
903 Saltzmann, N., Huggel, C., Rohrer, M., Silverio, W., Mark, B.G., Burns, P., Portocarrero, C.,
904 2013. Glacier changes and climate trends derived from multiple sources in the data
905 scarce Cordillera Vilcanota region, Southern Peruvian Andes. *The Cryosphere* 7, 103–118.
906 http://dx.doi.org/10.5194/tc-7-103-2013.
907
908 Schneider, C., and Gies, D., 2004. Effects of El Niño-southern oscillation on southernmost South
909 America precipitation at 53°S revealed from NCEP–NCAR reanalysis and weather station data.
910 *Int. J. Climatol.,* 24, 1057–1076.
911
912 Sparnocchia, S., Pinardi, N., and Demirov, E., 2003. Multivariate Empirical Orthogonal Function
913 analysis of the upper thermocline structure of the Mediterranean Sea from observations and
914 model simulations. *Ann. Geophys.*, 21, 167–187.
915

916 Vaughan, D. G., and Coauthors, 2013. Observations: Cryosphere. Climate Change 2103: The
917 Physical Science Basis, T. F. Stocker, et al., Cambridge University Press, 317–382.
918
919 Veettil, B.K., Maier, E.L.B., Bremer, U.F., and de Souza, 2014. Combined influence of PDO and
920 ENDO on Northern Andean glaciers: a case study on the Cotopaxi ice-covered volcano,
921 Ecuador. *Clim. Dyn.*, http://dx.doi.org/10.1007/s00382-014-2114-8.
922
923 Wolter, K. and Timlin, M. S. 2011. El Niño/Southern Oscillation behaviour since 1871 as
924 diagnosed in an extended multivariate ENSO index (MEI.ext). *International Journal of*
925 *Climatology,* 31(7), 1074–1087.
926
927 World Glacier Monitoring Service 2013. Glacier Mass Balance Bulletin 2010-2011 (Vol. 12),
928 edited by: Zemp, M., Nussbaumer, S.U., Naegeli, K., Gärtner-Roer, I., Paul, F., Hoelzle, M. and
929 Haeberli, W., ICSU (WDS) / IUGG (IACS) / UNEP / UNESCO / WMO, World Glacier
930 Monitoring Service, Zurich, Switzerland, 106 pp., publication based on database version: doi:
931 10.5904/wgms-fog-2013-11.
932
933 Yuan, X. J. and Martinson, D. G. 2000. Antarctic sea ice extent variability and its global
934 connectivity. *Journal of Climate*, 13(10), 1697–1717.
935
936 Yuan, X. J. and Martinson, D. G. 2001. The Antarctic dipole and its predictability. *Geophysical*
937 *Research Letters*, 28(18), 3609–3612.
938
939 Zhang, Y., Wallace, J. M., and Battisti, D. S. 1997. ENSO-like inter-decadal variability: 1900–
940 93. *Journal of Climate*, 10, 1004–1020, doi.org/10.1175/1520-0442(1997).
941
942
943
944
945
946

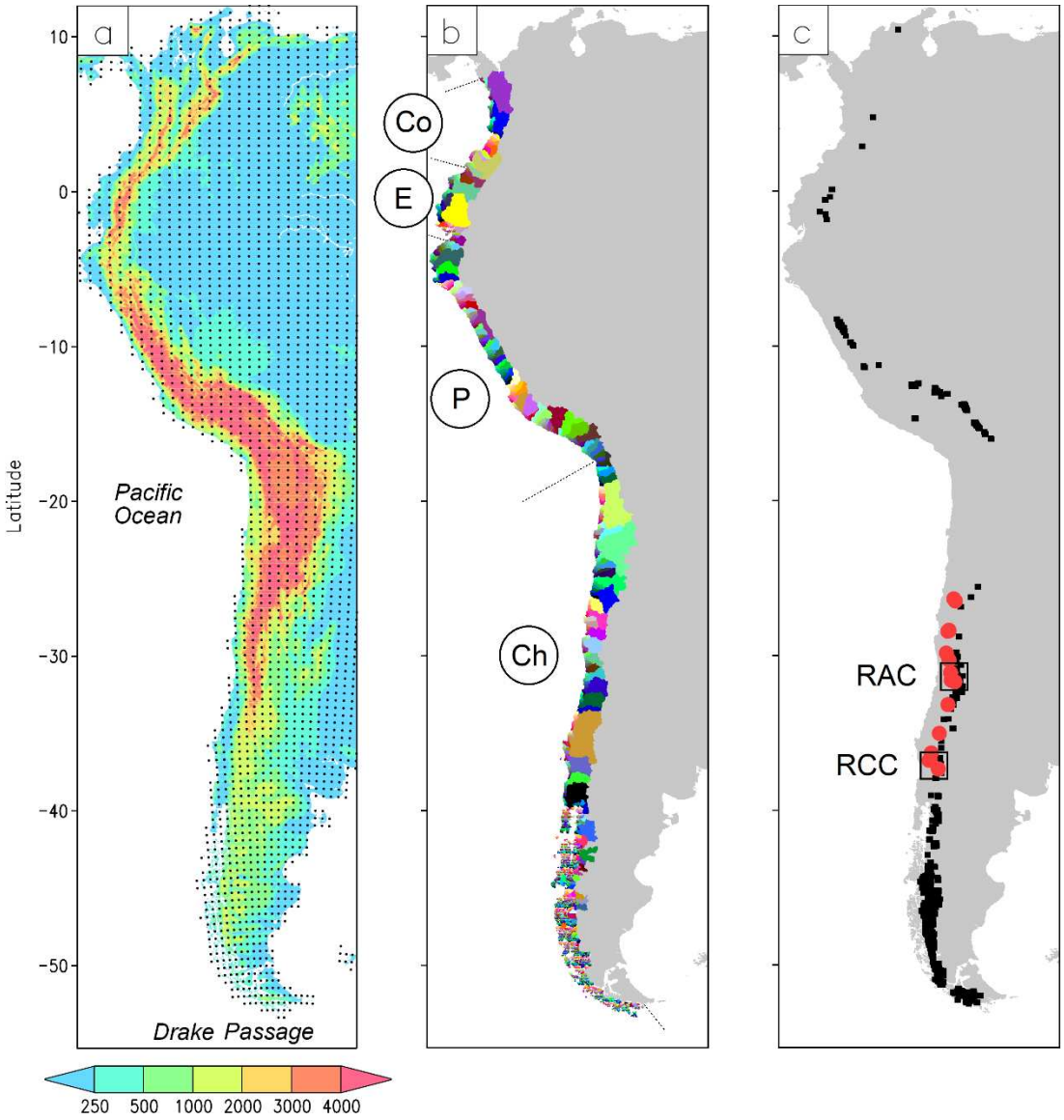

Figure 1: Western part of South America: (a) Topography (m, color increment is not linear) and locations of MERRA atmospheric forcing grid points used in the model simulations (black dots); (b) simulated individual drainage basins (represented by multiple colors) west of the continental divide draining to the Pacific Ocean. The borders are highlighted by straight lines between the countries Colombia (Co), Ecuador (E), Peru (P), and Chile (Ch); and (c) 16 hydrometric stations (red dots) in Chile (operated by Direction General de Aguas) used for verification of simulated river runoff. Glaciers are represented by black squares (added 20-km to the edges of each glacier to make them more visible in the figure). Also, two specific regions are illustrated from where examples of basin runoff and hydrographs are illustrated (see bold square): Rio Aconcagua en Chacabuquito (RAC) and Rio Cautin en Cajon (RCC).

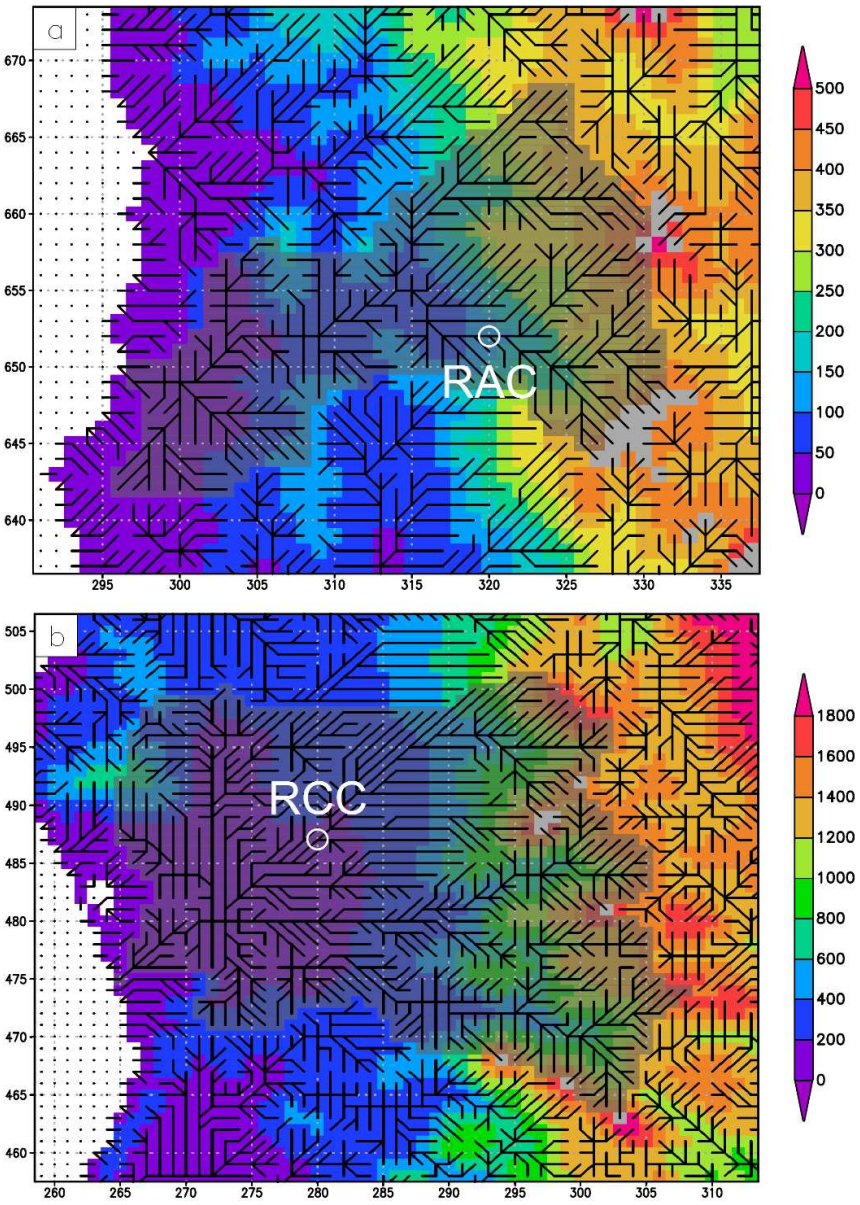

Figure 2: Examples of flow networks calculated from gridded topography and ocean-mask datasets to illustrate the HydroFlow network configuration over the simulation domain for the basins including: (a) the Rio Aconcagua en Chacabuquito (RAC) hydrographic station; and (b) the Rio Cautin en Cajon (RCC) hydrological station. The hydrological stations are marked with a white circle, the flow network with black lines, and the basin with a transparent shaded gray of which drains into the ocean (white color). Glaciers are represented by light gray squares and topography by multiple colors.

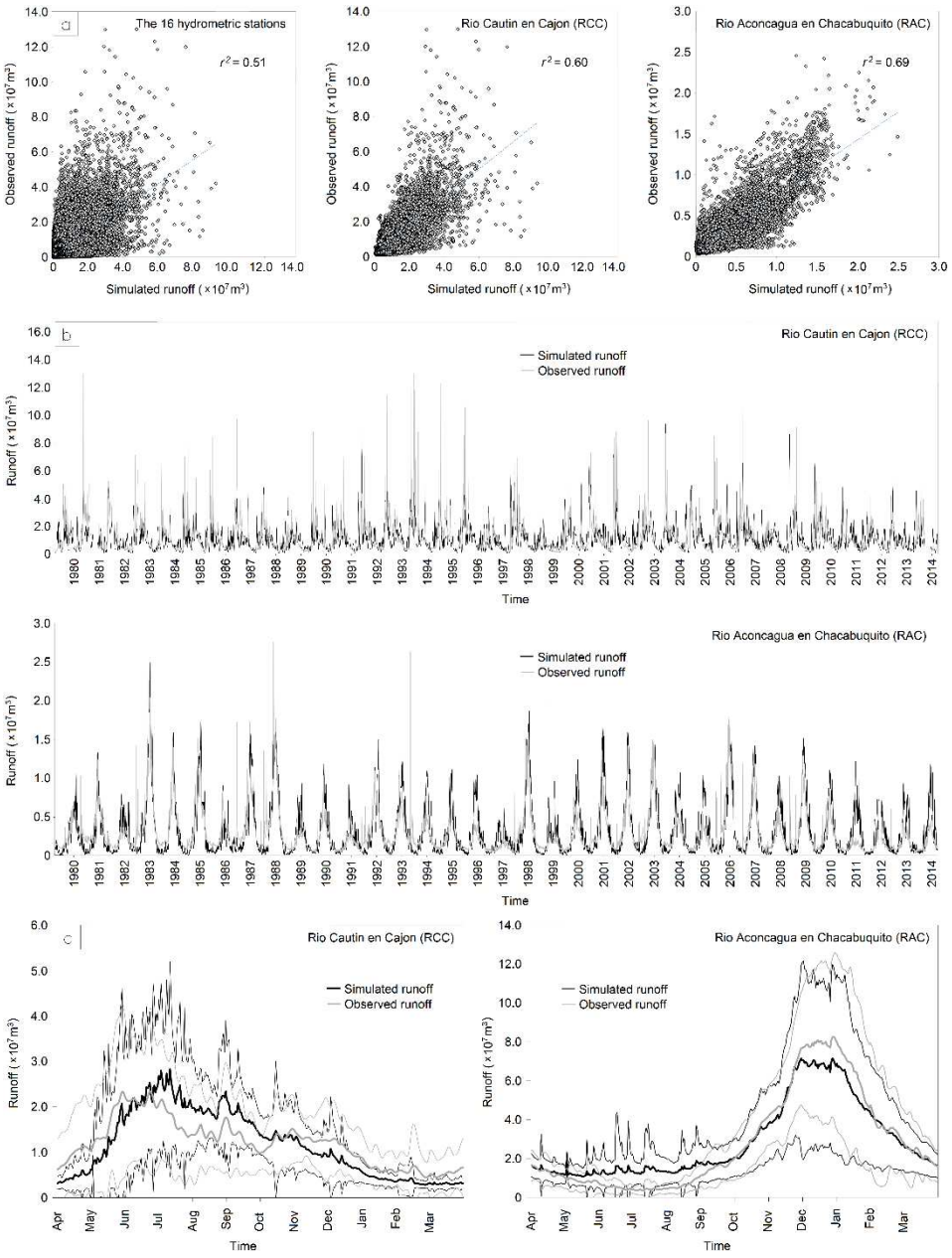

966

967 **Figure 3:** (a) A comparison between daily simulated runoff and observed runoff for 16
968 hydrometric stations and an example of two of the individual stations Rio Cautin en Cajon and
969 Rio Aconcagua en Chacabuquito (1 April 1979 through 31 March 2014); (b) daily simulated and
970 observed runoff time series from Rio Cautin en Cajon and Rio Aconcagua en Chacabuquito; (c)
971 mean seasonal hydrographs (bold lines) 1979–2014 including time series of one standard
972 deviation (thin lines) for the two individual stations Rio Cautin en Cajon and Rio Aconcagua en
973 Chacabuquito.

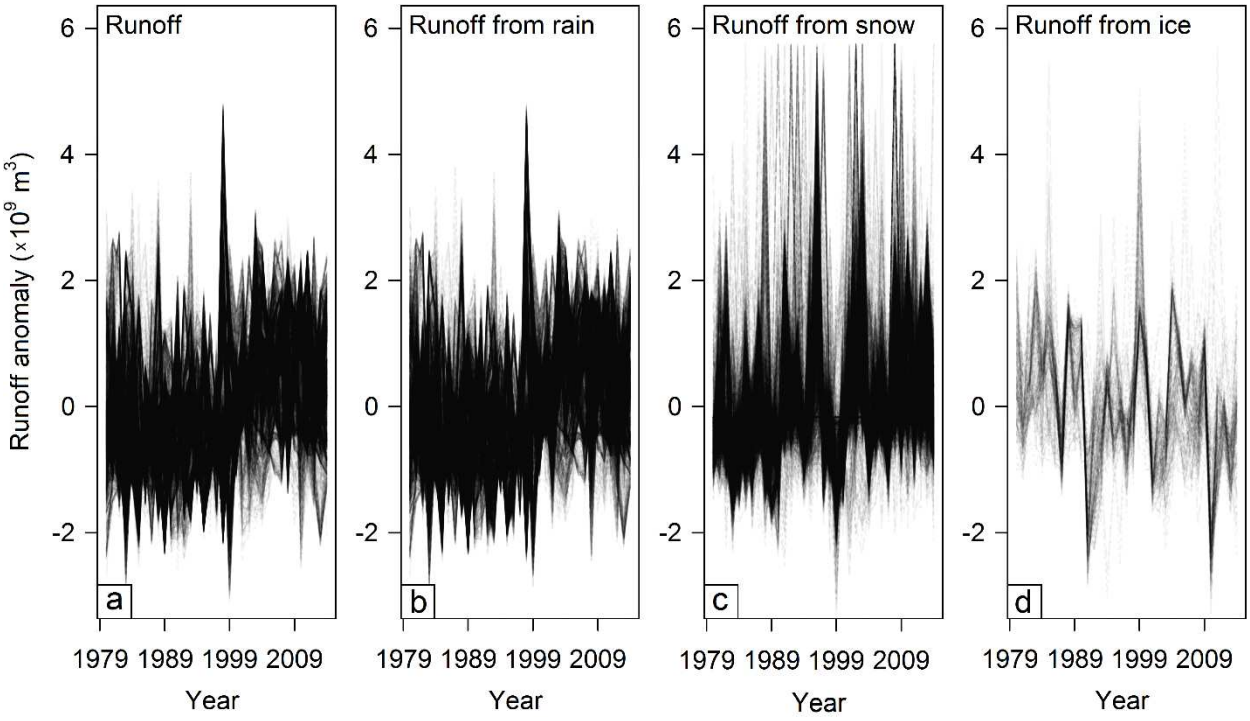

974

975 **Figure 4:** Time series of simulated annual runoff anomaly from each individual drainage basin
976 west of the continental divide for the period 1979–2014: (a) total runoff; (b) runoff from rain; (c)
977 runoff from snowmelt; and (d) runoff from ice melt.

978

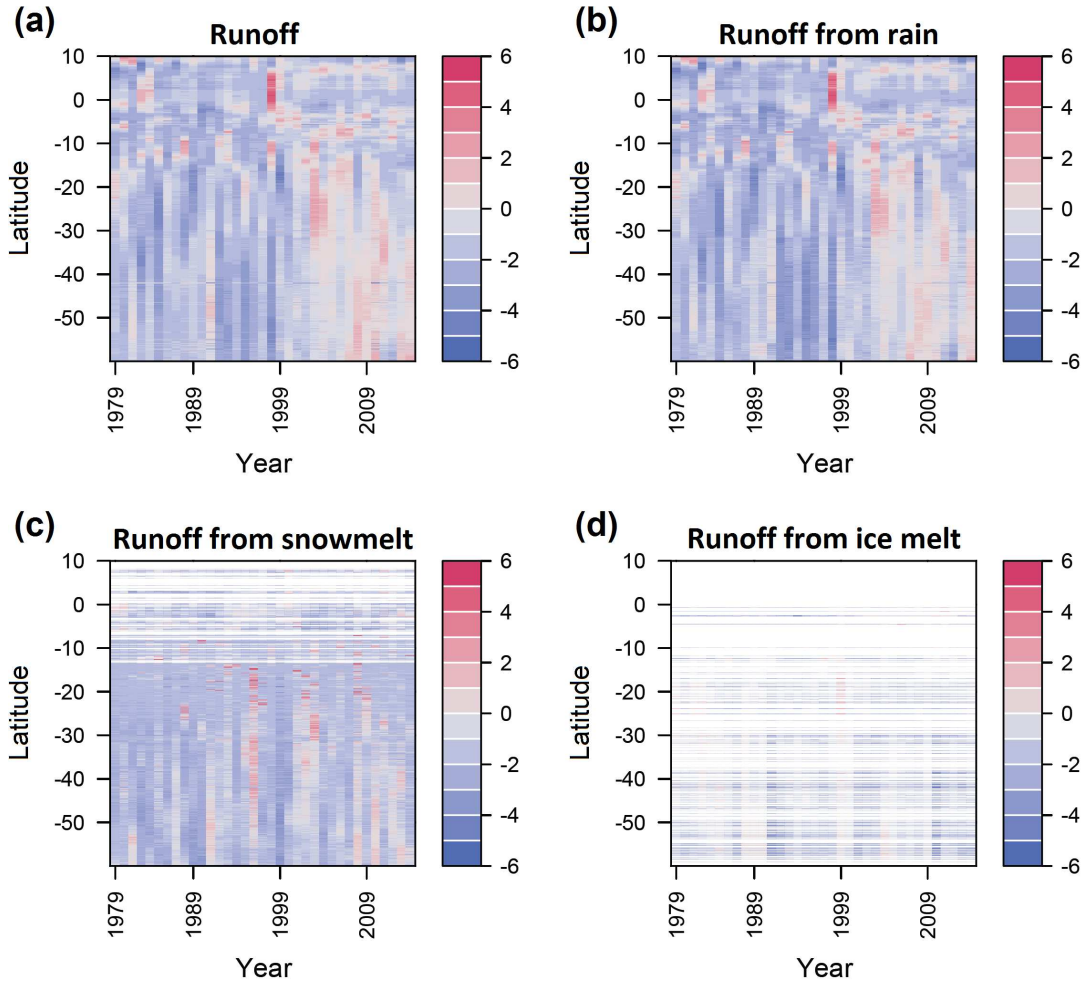

Figure 5: A 'field' representation of the scaled and centered, simulated runoff data indexed by latitude and year (1979–2014): (a) total runoff; (b) runoff from rain; (c) runoff from snowmelt; and (d) runoff from ice melt. The scale bar indicates runoff values above and below average (e.g., the data were centered at 0).

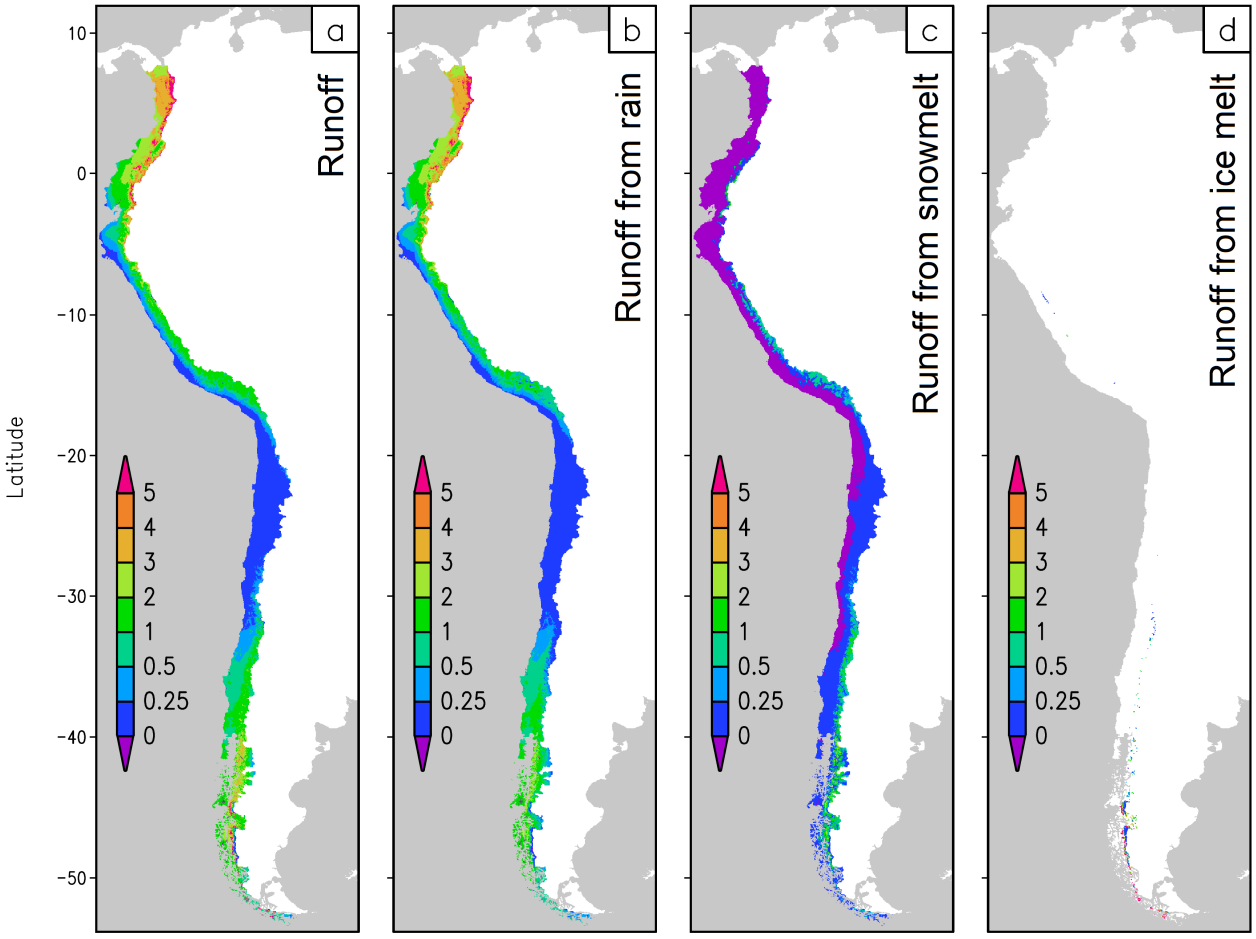

Figure 6: Simulated 35-year average runoff in each grid cell west of the continental divide (m w.e., color increment is not linear): (a) total annual runoff ; (b) annual runoff from rain; (c) annual runoff from snowmelt; and (d) annual runoff from ice melt.

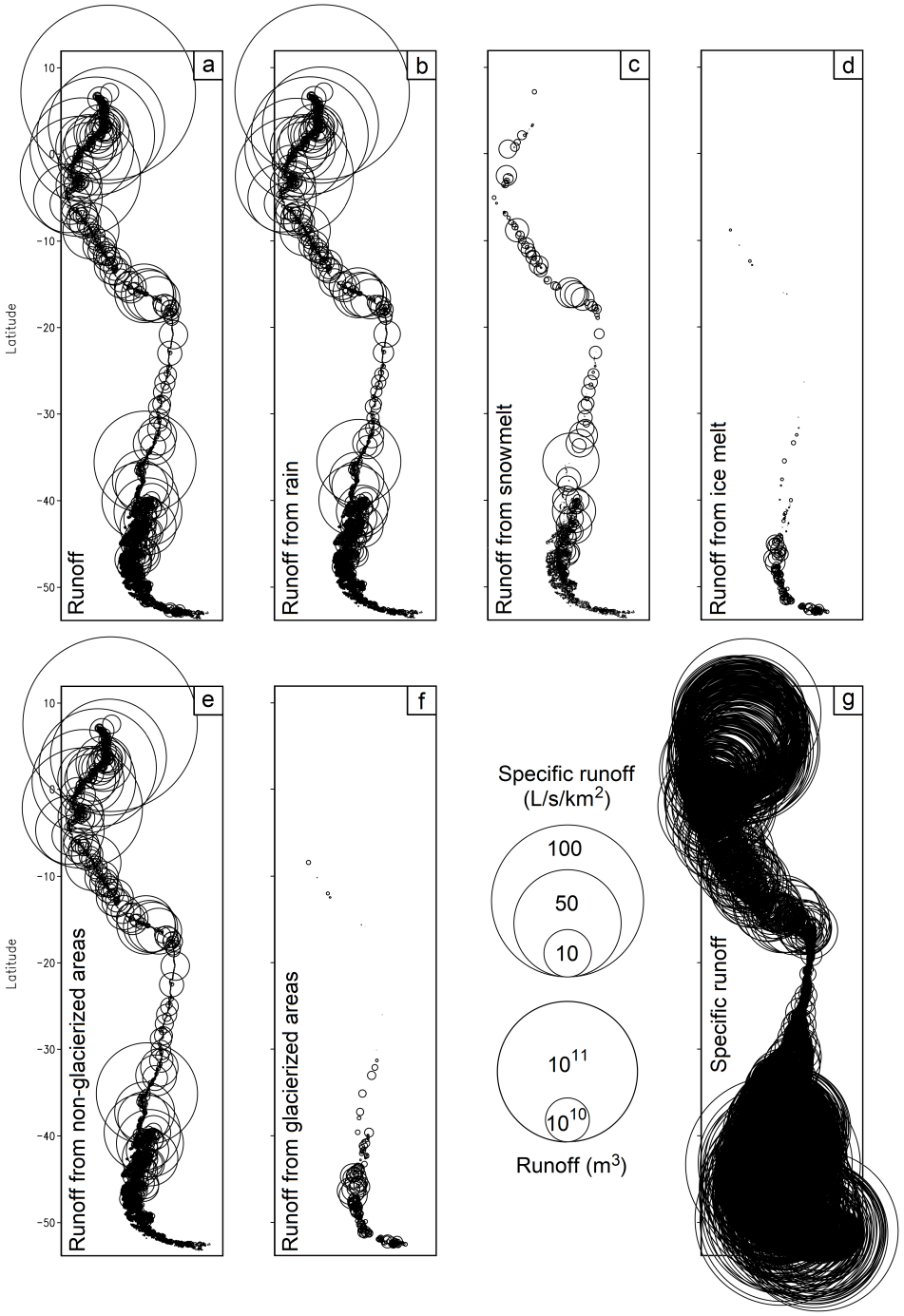

Figure 7: Simulated 35-year average annual runoff from each individual drainage basins west of the continental divide (the area of each circle is proportional to the runoff): (a) total runoff; (b) runoff from rain; (c) runoff from snowmelt; (d) runoff from ice melt; (e) runoff from non-glacierized areas; (f) runoff from glacierized areas; and (g) specific runoff.

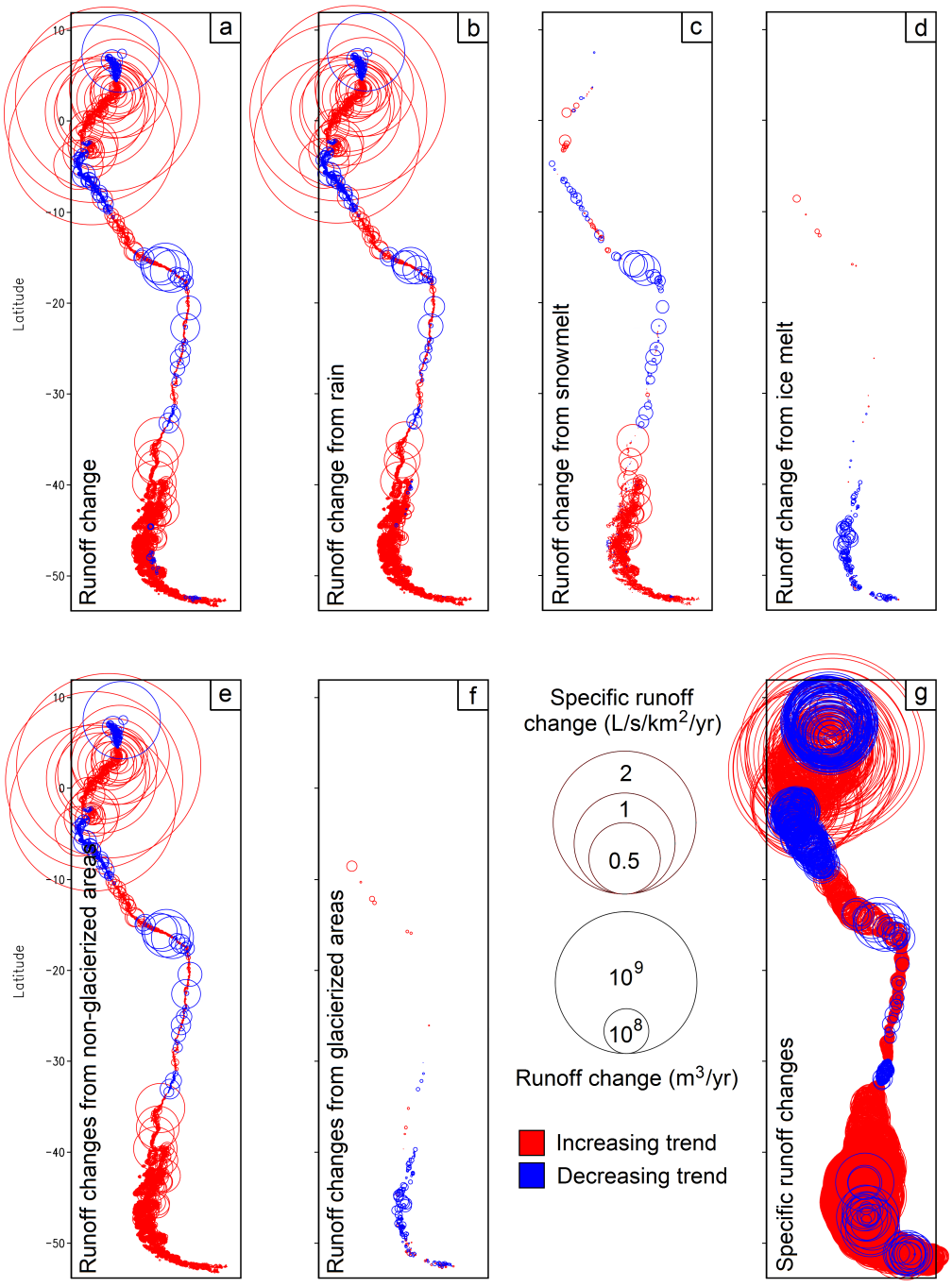

Figure 8: Simulated 35-year annual changes in runoff from each individual drainage basins west of the continental divide (the area of each circle is proportional to the runoff): (a) total runoff change; (b) runoff change from rain; (c) runoff change from snowmelt; (d) runoff change from glacier ice melt; (e) runoff change from non-glacierized areas; (f) runoff change from glacierized areas; and (g) specific runoff change.

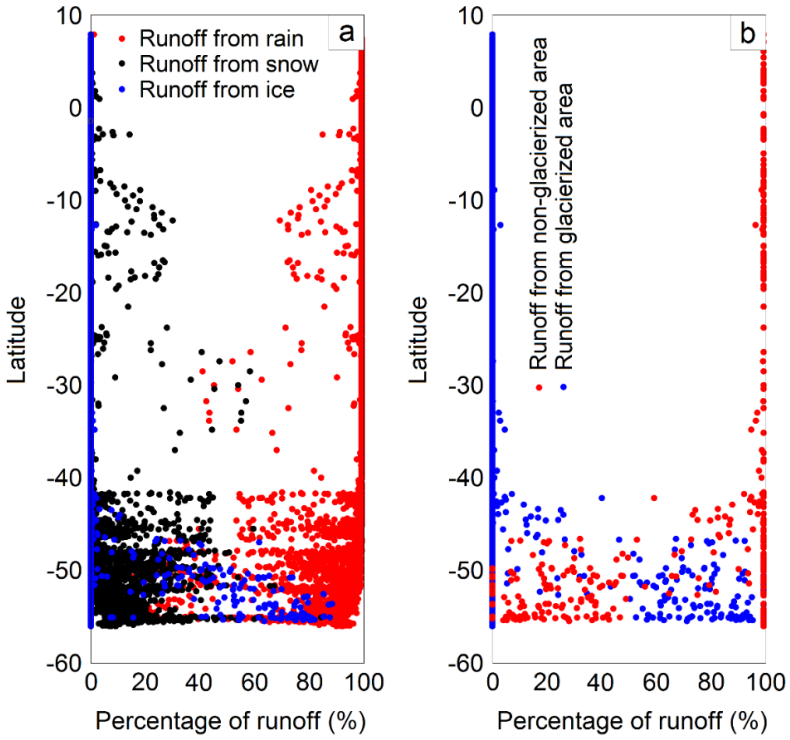

Figure 9: The percentage of seasonal basin runoff versus latitude for (a) runoff from rain, snowmelt, and ice melt; and (b) runoff from non-glacierized areas and glacierized areas.

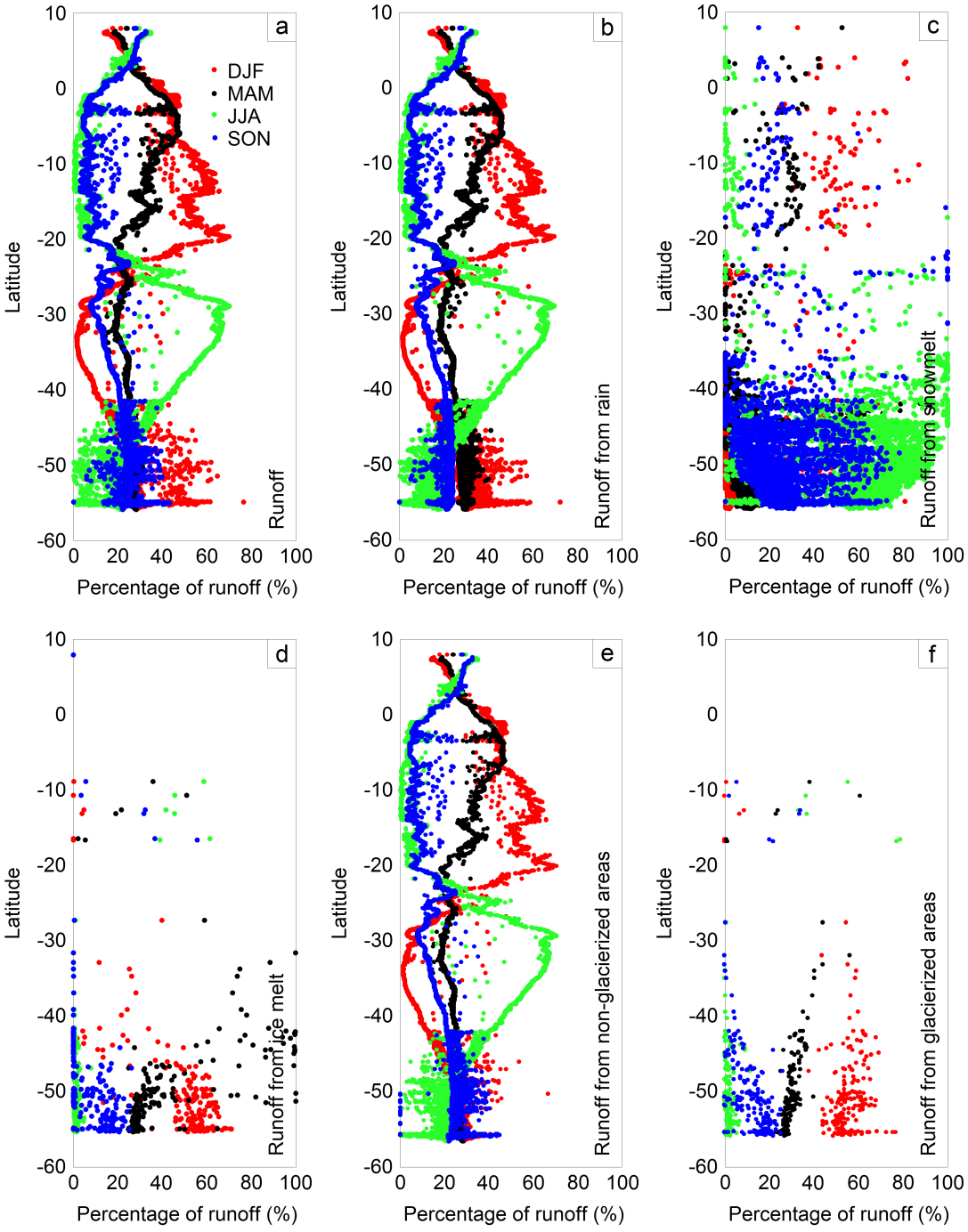

1025

1026 **Figure 10:** The percentage of seasonal basin runoff versus latitude for (a) runoff; (b) runoff from
1027 rain; (c) runoff from snowmelt; (d) runoff from ice melt; (e) runoff from non-glacierized areas;
1028 and (f) runoff from glacierized areas. The seasons are divided into three-month intervals:
1029 December, January, and February (DJF); March, April, and May (MAM), June, July, and August
1030 (JJA); and September, October, and November (SON).

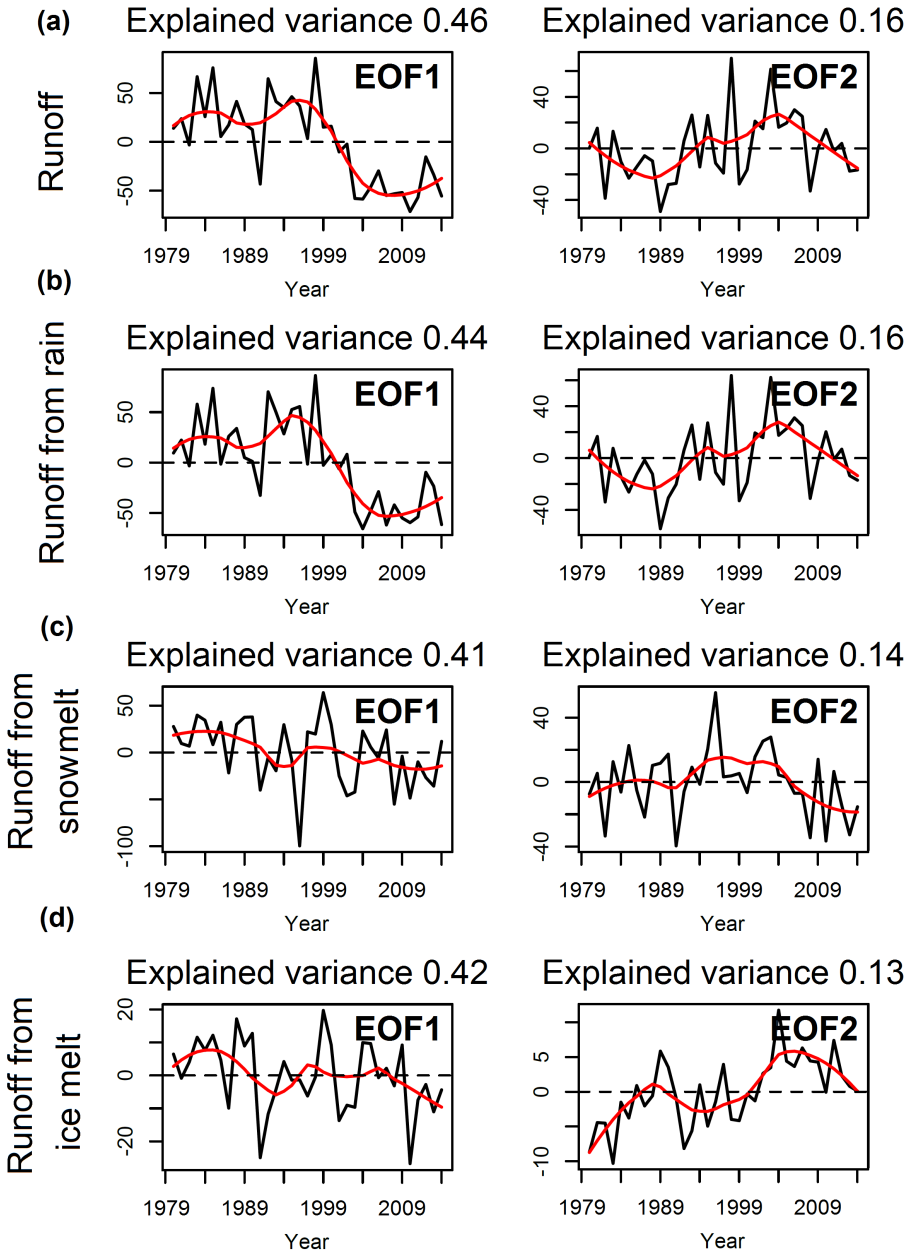

Figure 11: Simulated runoff time series (1979–2014) of the empirical orthogonal functions (black curve) and 5-years running mean smoothing line (red curve) of EOF1 and EOF2 for (a) total runoff; (b) runoff from rain; (c) runoff from snowmelt; and (d) runoff from ice melt. The explained variance is shown for each EOF.

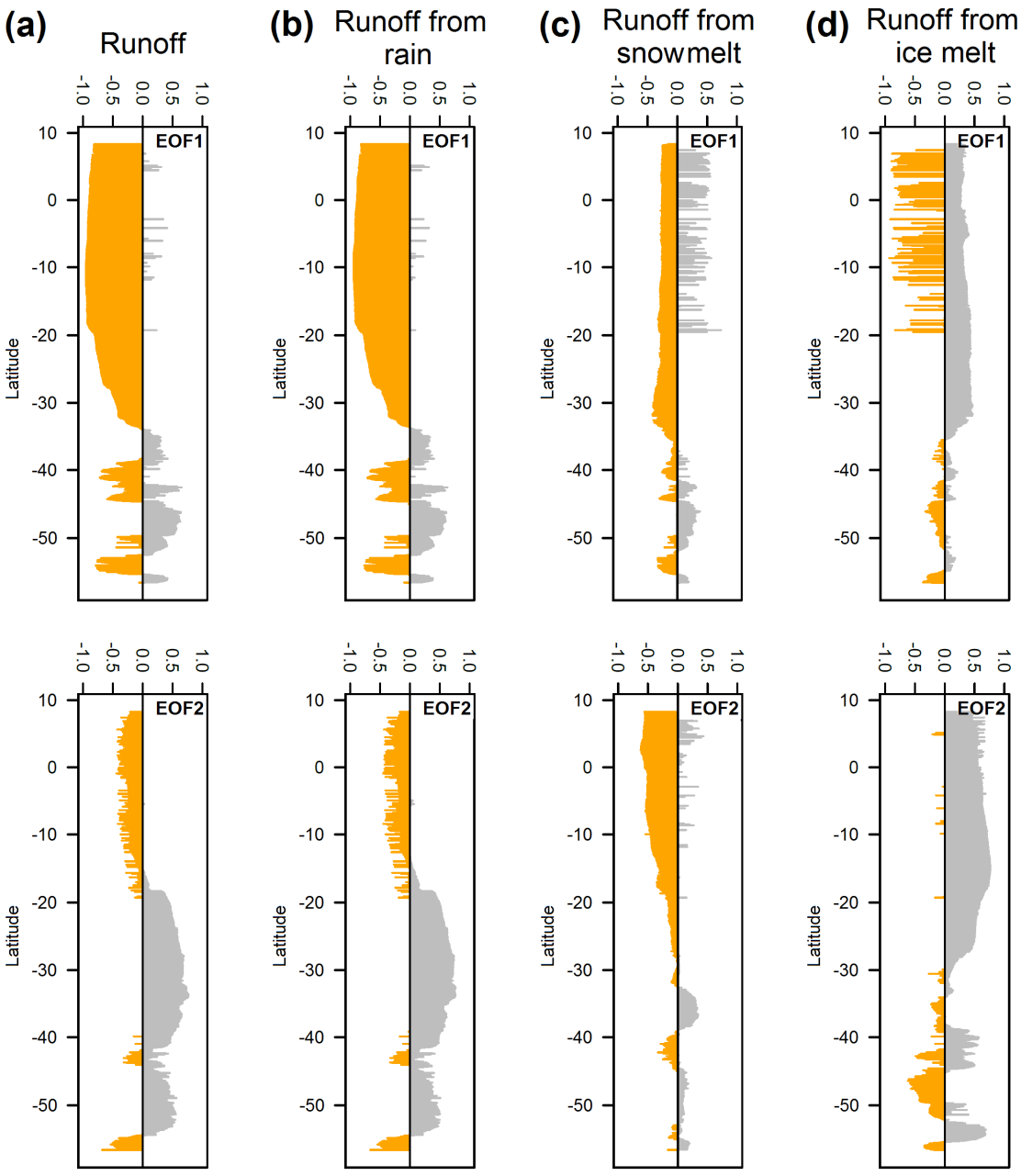

Figure 12: Eigenvector correlation values for each individual site for EOF1 and EOF2: (a) runoff; (b) runoff from rain; (c) runoff from snowmelt; and (d) runoff from ice melt.

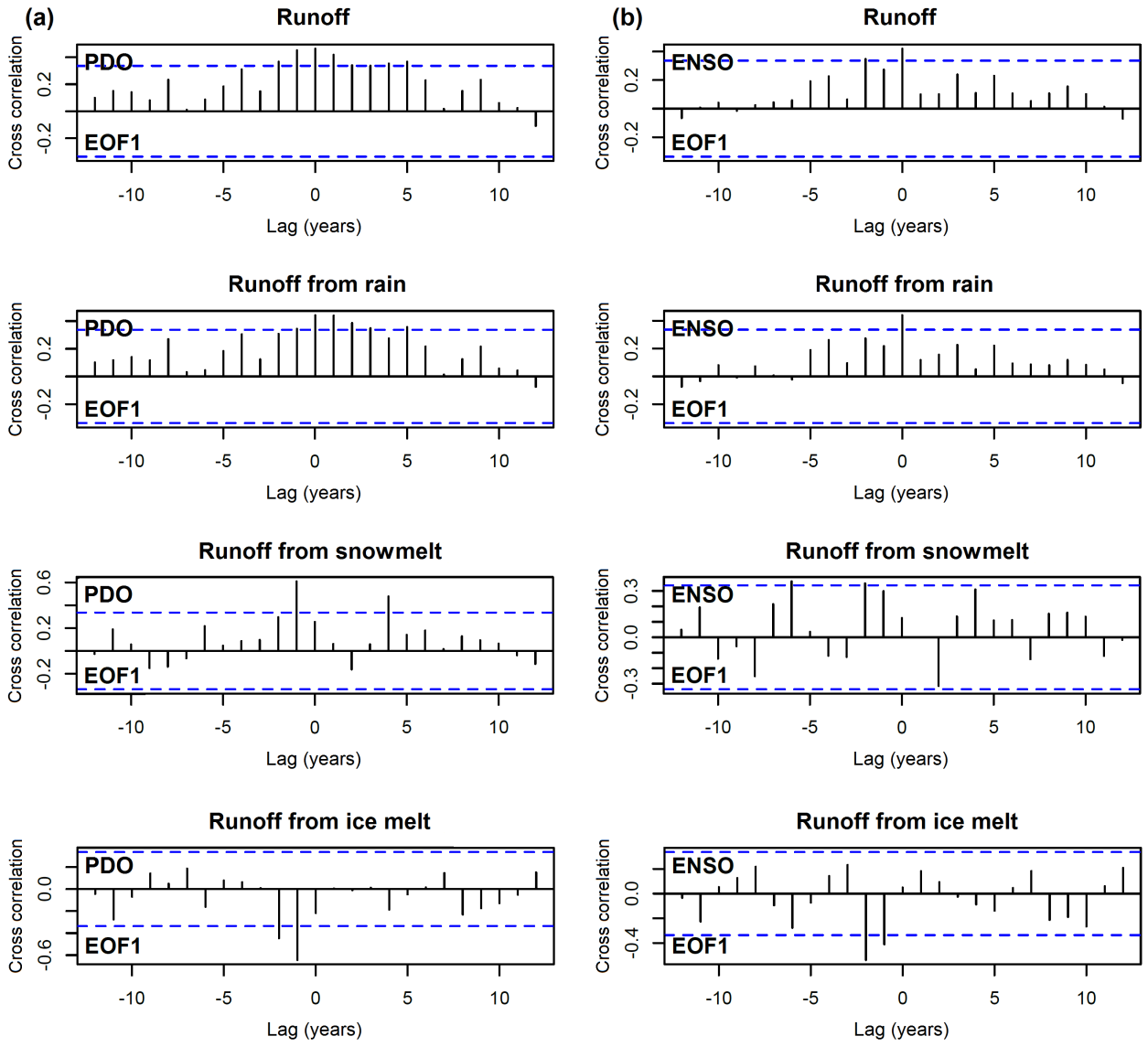

Figure 13: EOF1 cross correlation relationships between (a) PDO and (b) ENSO for runoff, runoff from rain, runoff from snowmelt, and runoff from ice melt. The horizontal dashed lines indicate the line of significance (95% confidence).

Table 1: Example of statistical information regarding daily simulated runoff and observed runoff from 16 hydrometric stations and the two individual hydrometric stations Rio Cautin en Cajon and Rio Aconcagua en Chacabuquito. The brackets indicate how much simulated runoff is overestimated compared to observed runoff.

	Sixteen hydrometric stations		Rio Cautin en Cajon		Rio Aconcagua en Chacabuquito	
	Simulated runoff	Observed runoff	Simulated runoff	Observed runoff	Simulated runoff	Observed runoff
Average ($\times 10^7$ m^3)	0.33 (13 %)	0.29	1.21 (3 %)	1.17	0.32 (9 %)	0.29
Standard deviation ($\times 10^7$ m^3)	0.56	0.58	1.02	1.14	0.35	0.28
r^2	0.52		0.60		0.69	
r^2-range	0.31–0.71		-------		-------	

Table 2: Simulated annual mean runoff and standard deviation (standard deviation is presented for the 35-year mean period) for the four countries Colombia, Ecuador, Peru, and Chile from 1979 through 2014, and on pentadal scale. The linear trends in runoff are highlighted in brackets.

	Parameters (m^3)	Colombia	Ecuador	Peru	Chile*	Total (domain)
1979/80–1983/84	Runoff	38.0×10^{10}	16.6×10^{10}	24.5×10^{10}	50.3×10^{10}	129.4×10^{10}
	Runoff from rain	37.8×10^{10} (99 %)	16.1×10^{10} (97 %)	21.0×10^{10} (86 %)	35.2×10^{10} (70 %)	111.2×10^{10} (86 %)
	Runoff from snowmelt	0.1×10^{10} (<1 %)	0.5×10^{10} (3 %)	3.5×10^{10} (14 %)	11.1×10^{10} (22 %)	15.2×10^{10} (12 %)
	Runoff from ice melt	0.1×10^{10} (<1 %)	$<0.1\times10^{10}$ (<1 %)	$<0.1\times10^{10}$ (<1 %)	4.0×10^{10} (8 %)	3.0×10^{10} (2 %)
	Runoff from non-glacierized areas	38.0×10^{10} (>99 %)	16.6×10^{10} (>99 %)	24.5×10^{10} (>99 %)	43.3×10^{10} (86 %)	122.4×10^{10} (95 %)
	Runoff from glacierized areas	$<0.1\times10^{10}$ (<1 %)	$<0.1\times10^{10}$ (<1 %)	$<0.1\times10^{10}$ (<1 %)	7.0×10^{10} (14 %)	7.0×10^{10} (5 %)
1984/85–1988/89	Runoff	37.8×10^{10}	15.3×10^{10}	22.7×10^{10}	48.9×10^{10}	124.7×10^{10}
	Runoff from rain	37.6×10^{10} (99 %)	14.7×10^{10} (96 %)	19.2×10^{10} (85 %)	33.5×10^{10} (69 %)	105.2×10^{10} (84 %)
	Runoff from snowmelt	0.1×10^{10} (<1 %)	0.6×10^{10} (4 %)	3.5×10^{10} (15 %)	11.5×10^{10} (24 %)	15.7×10^{10} (13 %)
	Runoff from ice melt	0.1×10^{10} (<1 %)	$<0.1\times10^{10}$ (<1 %)	$<0.1\times10^{10}$ (<1 %)	3.9×10^{10} (7 %)	3.8×10^{10} (3 %)
	Runoff from non-glacierized areas	37.8×10^{10} (>99 %)	15.3×10^{10} (>99 %)	22.7×10^{10} (>99 %)	42.1×10^{10} (86 %)	117.9×10^{10} (95 %)
	Runoff from glacierized areas	$<0.1\times10^{10}$ (<1 %)	$<0.1\times10^{10}$ (<1 %)	$<0.1\times10^{10}$ (<1 %)	6.8×10^{10} (14 %)	6.8×10^{10} (5 %)
1989/90–1993/94	Runoff	3.5×10^{11}	15.8×10^{10}	22.6×10^{10}	49.5×10^{10}	123.0×10^{10}
	Runoff from rain	3.5×10^{11} (99 %)	15.2×10^{10} (96 %)	19.3×10^{10} (85 %)	34.0×10^{10} (69 %)	103.5×10^{10} (84 %)
	Runoff from snowmelt	0.1×10^{10} (<1 %)	0.6×10^{10} (4 %)	3.3×10^{10} (15 %)	12.1×10^{10} (24 %)	16.1×10^{10} (13 %)
	Runoff from ice melt	0.1×10^{10} (<1 %)	$<0.1\times10^{10}$ (<1 %)	$<0.1\times10^{10}$ (<1 %)	3.4×10^{10} (7 %)	3.4×10^{10} (3 %)
	Runoff from non-glacierized areas	3.5×10^{11} (>99 %)	15.8×10^{10} (>99 %)	22.6×10^{10} (>99 %)	43.1×10^{10} (87 %)	116.6×10^{10} (95 %)
	Runoff from glacierized areas	$<0.1\times10^{10}$ (<1 %)	$<0.1\times10^{10}$ (<1 %)	$<0.1\times10^{10}$ (<1 %)	6.4×10^{10} (13 %)	6.4×10^{10} (5 %)
1994/95–1998/99	Runoff	39.4×10^{10}	21.2×10^{10}	25.4×10^{10}	48.2×10^{10}	134.2×10^{10}
	Runoff from rain	39.3×10^{10} (99 %)	20.7×10^{10} (98 %)	22.0×10^{10} (87 %)	33.1×10^{10} (69 %)	115.1×10^{10} (86 %)
	Runoff from snowmelt	0.1×10^{10} (<1 %)	0.5×10^{10} (2 %)	3.4×10^{10} (13 %)	11.3×10^{10} (23 %)	15.3×10^{10} (12 %)
	Runoff from ice melt	$<0.1\times10^{10}$ (<1 %)	$<0.1\times10^{10}$ (<1 %)	$<0.1\times10^{10}$ (<1 %)	3.8×10^{10} (8 %)	3.8×10^{10} (2 %)
	Runoff from non-glacierized areas	39.4×10^{10} (>99 %)	21.2×10^{10} (>99 %)	25.4×10^{10} (>99 %)	41.6×10^{10} (86 %)	127.6×10^{10} (95 %)
	Runoff from glacierized areas	$<0.1\times10^{10}$ (<1 %)	$<0.1\times10^{10}$ (<1 %)	$<0.1\times10^{10}$ (<1 %)	6.6×10^{10} (14 %)	6.6×10^{10} (5 %)
1999/2000–2003/04	Runoff	43.3×10^{10}	25.4×10^{10}	21.8×10^{10}	54.4×10^{10}	144.9×10^{10}
	Runoff from rain	43.1×10^{10} (99 %)	24.7×10^{10} (97 %)	19.0×10^{10} (87 %)	37.6×10^{10} (69 %)	124.5×10^{10} (86 %)
	Runoff from snowmelt	0.1×10^{10} (<1 %)	0.6×10^{10} (2 %)	2.8×10^{10} (13 %)	13.5×10^{10} (25 %)	16.9×10^{10} (12 %)
	Runoff from ice melt	0.1×10^{10} (<1 %)	0.1×10^{10} (1 %)	$<0.1\times10^{10}$ (<1 %)	3.3×10^{10} (6 %)	3.5×10^{10} (2 %)
	Runoff from non-glacierized areas	43.3×10^{10} (>99 %)	25.4×10^{10} (>99 %)	21.8×10^{10} (>99 %)	48.1×10^{10} (88 %)	138.5×10^{10} (96 %)
	Runoff from glacierized areas	$<0.1\times10^{10}$ (<1 %)	$<0.1\times10^{10}$ (<1 %)	$<0.1\times10^{10}$ (<1 %)	6.3×10^{10} (12 %)	6.4×10^{10} (4 %)
2004/05–2008/09	Runoff	45.5×10^{10}	26.6×10^{10}	22.5×10^{10}	55.8×10^{10}	150.4×10^{10}
	Runoff from rain	45.4×10^{10} (99 %)	26.0×10^{10} (98 %)	19.6×10^{10} (87 %)	38.7×10^{10} (69 %)	129.8×10^{10} (86 %)
	Runoff from snowmelt	0.1×10^{10} (<1 %)	0.6×10^{10} (2 %)	2.9×10^{10} (13 %)	13.3×10^{10} (24 %)	16.9×10^{10} (11 %)
	Runoff from ice melt	$<0.1\times10^{10}$ (<1 %)	$<0.1\times10^{10}$ (<1 %)	$<0.1\times10^{10}$ (<1 %)	3.8×10^{10} (7 %)	3.7×10^{10} (3 %)
	Runoff from non-glacierized areas	45.5×10^{10} (>99 %)	26.6×10^{10} (>99 %)	22.5×10^{10} (>99 %)	48.6×10^{10} (87 %)	143.3×10^{10} (95 %)
	Runoff from glacierized areas	$<0.1\times10^{10}$ (<1 %)	$<0.1\times10^{10}$ (<1 %)	$<0.1\times10^{10}$ (<1 %)	7.2×10^{10} (13 %)	7.1×10^{10} (4 %)
2009/10–2013/14	Runoff	47.5×10^{10}	26.3×10^{10}	23.1×10^{10}	52.0×10^{10}	148.9×10^{10}
	Runoff from rain	47.4×10^{10} (99 %)	25.7×10^{10} (98 %)	19.9×10^{10} (86 %)	36.2×10^{10} (70 %)	129.3×10^{10} (87 %)
	Runoff from snowmelt	0.1×10^{10} (<1 %)	0.6×10^{10} (2 %)	3.2×10^{10} (14 %)	12.6×10^{10} (24 %)	16.5×10^{10} (11 %)
	Runoff from ice melt	$<0.1\times10^{10}$ (<1 %)	$<0.1\times10^{10}$ (<1 %)	$<0.1\times10^{10}$ (<1 %)	3.2×10^{10} (6 %)	3.1×10^{10} (2 %)
	Runoff from non-glacierized areas	47.5×10^{10} (>99 %)	26.3×10^{10} (>99 %)	23.1×10^{10} (>99 %)	45.7×10^{10} (88 %)	142.5×10^{10} (96 %)
	Runoff from glacierized areas	$<0.1\times10^{10}$ (<1 %)	$<0.1\times10^{10}$ (<1 %)	$<0.1\times10^{10}$ (<1 %)	6.3×10^{10} (12 %)	6.4×10^{10} (4 %)
1979/80–2013/14	Runoff	$40.9 \pm 5.60\times10^{10}$ (30 %)	$21.0 \pm 5.63\times10^{10}$ (15 %)	$23.3 \pm 2.58\times10^{10}$ (17 %)	$51.3 \pm 4.09\times10^{10}$ (38 %)	$136.5 \pm 12.15\times10^{10}$
		(0.37×10^{10} m^3 yr^{-1})	(0.43×10^{10} m^3 yr^{-1})	(-0.03×10^{10} m^3 yr^{-1})	(0.17×10^{10} m^3 yr^{-1})	(0.94×10^{10} m^3 yr^{-1})
	Runoff from rain	40.8×10^{10} (99 %)	20.4×10^{10} (97 %)	20.0×10^{10} (86 %)	35.5×10^{10} (69 %)	116.9×10^{10} (86 %)
		(0.37×10^{10} m^3 yr^{-1})	(0.43×10^{10} m^3 yr^{-1})	(-0.02×10^{10} m^3 yr^{-1})	(0.12×10^{10} m^3 yr^{-1})	(0.88×10^{10} m^3 yr^{-1})
	Runoff from snowmelt	0.1×10^{10} (<1 %)	0.6×10^{10} (3 %)	3.2×10^{10} (14 %)	12.2×10^{10} (24 %)	16.1×10^{10} (12 %)
		($<0.01\times10^{10}$ m^3 yr^{-1})	($<0.01\times10^{10}$ m^3 yr^{-1})	(-0.01×10^{10} m^3 yr^{-1})	(0.07×10^{10} m^3 yr^{-1})	(0.05×10^{10} m^3 yr^{-1})
	Runoff from ice melt	$<0.1\times10^{10}$ (<1 %)	$<0.1\times10^{10}$ (<1 %)	0.1×10^{10} (<1 %)	3.6×10^{10} (7 %)	3.5×10^{10} (2 %)
		($<0.01\times10^{10}$ m^3 yr^{-1})	($<0.01\times10^{10}$ m^3 yr^{-1})	($<0.01\times10^{10}$ m^3 yr^{-1})	(-0.02×10^{10} m^3 yr^{-1})	(0.01×10^{10} m^3 yr^{-1})
	Runoff from non-glacierized areas	40.9×10^{10} (>99 %)	21.0×10^{10} (>99 %)	23.3×10^{10} (>99 %)	44.6×10^{10} (87 %)	129.8×10^{10} (95 %)
	Runoff from glacierized areas	$<0.1\times10^{10}$ (<1 %)	$<0.1\times10^{10}$ (<1 %)	$<0.1\times10^{10}$ (<1 %)	6.7×10^{10} (13 %)	6.7×10^{10} (5 %)

* For Chile it is only the runoff draining into the Pacific Ocean and the Drake Passage.